An Electrical Detection System for in situ Characterization of Microbubbles in Flow Focusing Microfluidic Devices

---

A Thesis

Presented to

the faculty of the School of Engineering and Applied Science

University of Virginia

---

in partial fulfillment
of the requirements for the degree

Master of Science

by

John-Marschner Robert Rickel

August 2019

APPROVAL SHEET

This Thesis
is submitted in partial fulfillment of the requirements
for the degree of
Master of Science

Author Signature: 

This Thesis has been read and approved by the examining committee:

Advisor: John A. Hossack

Committee Member: Richard J. Price

Committee Member: Alexander L. Klibanov

Committee Member: _____

Committee Member: _____

Committee Member: _____

Accepted for the School of Engineering and Applied Science:

Craig H. Benson, School of Engineering and Applied Science

August 2019

Acknowledgements

I would like to acknowledge Mr. Johnny L. Chen, Mr. Sushanth Govinahallisathyanarayana, Dr. Ali H. Dhanaliwala, Dr. Adam J. Dixon, Dr. Joseph P. Kilroy, and Dr. Shiying Wang for their tremendous contributions to this thesis in terms of microfluidic device design and fabrication, electrical circuit design and considerations and experimental studies. Further, I would like to thank all the members of the Hossack lab for their suggestions, contributions, and support, including Ms. Elizabeth B. Herbst, Mr. Yanjun Xie, Dr. Frank W. Mauldin, Dr. Sunil Unnikrishnan, and Dr. Feifei Zhao.

Next, I would like to acknowledge my advisor, Dr. John A. Hossack for imparting indispensable mentorship and guidance toward my growth as a researcher and career. I would also like to thank Dr. Alexander L. Klibanov for our countless discussions and his guidance in the design of experiments presented in this thesis. Additionally, I thank Dr. Richard J. Price for his time, questions and suggestions in crafting this thesis. Further, I would like to recognize Dr. Song Hu and Dr. Craig H. Meyer, who both previously served on my dissertation committee, for their time and suggestions in shaping my thesis.

I would like to acknowledge Dr. Gary K. Owen for his mentorship and career guidance during my time in the Cardiovascular Research Center training program. Additionally, I thank Dr. Arthur W. Lichtenberger for his mentorship in the University of Virginia Microfabrication Laboratory.

I thank the Royal Society of Chemistry for permission to use the content and figures that comprise chapters 2 and 3, which was published in *Lab on a Chip*.

Finally, I thank my family for supporting me through this journey. I cherish the hard work, positive attitude and relentless effort that they display daily. They are wonderful examples that I strive to emulate.

This thesis was supported by NIH RO1 HL090700, S10 RR02733, and S10 RR025594 grants to the Hossack Lab as well as American Heart Association Predoctoral Research Fellowship and the University of Virginia Cardiovascular Research Center T32 Training Grant.

Abstract

Flow focusing microfluidic devices (FFMDs) have been investigated for the production of monodisperse populations of microbubbles for biomedical engineering applications. High-speed optical microscopy is commonly used to monitor FFMD microbubble production parameters, such as diameter and production rate, but this limits the scalability and portability of the approach. In this thesis, a novel FFMD design featuring integrated electronics for measuring microbubble diameters and production rates is presented. A micro Coulter Particle Counter (μCPC), using electrodes integrated within the expanding nozzle of an FFMD (FFMD-μCPC), was designed, fabricated and tested. Finite element analysis (FEA) of optimal electrode geometry was performed and validated with experimental data. Electrical data was collected for 8-20 μm diameter microbubbles at production rates up to 3.25×10^5 MB s^{-1} and compared to both high-speed microscopy data and FEA simulations. Within a valid operating regime, Coulter counts of microbubble production rates matched optical reference values. The Coulter method agreed with the optical reference method in evaluating the microbubble diameter to a coefficient of determination of $R^2 = 0.91$.

Table of Contents

List of Figures

List of Tables

List of Equations

List of Software

List of Nomenclature

Mathematical Symbols

Symbol	Description
b	coefficients
c	coefficients for
C2C	centre-to-centre distance
CF	correction factor
Ø	diameter
D_E	electrically determined microbubble diameter
$D_{E,corrected}$	corrected electrically determined microbubble diameter
D_O	optically determined microbubble diameter
°	degree
E	electric field
EL_D	detection region electrodes
EL_R	reference arm electrodes
ε_r	relative permativity
FFR	fluid flow rate
G_{AVG}	gain (determined empirically for system)
∇	gradient
J	current density (volume)
J_E	current density (electric field)
PR	production rate
PR_E	electrically determined production rate
PR_O	optically determined production rate
Q_J	electric charge
σ	electrical conductivity
G_{AVG}	gain determined for system
R	Resistance
ΔR	Resistance change
V	electric potential
V_{pp}	voltage peak-to-peak
ΔV	voltage change
x	downstream position in microfluidic channel
Z	impedance

Acronyms

Acronym	Description
3D	Three-dimensional
AC	Alternating current
CDT	Catheter-directed thrombolysis
DC	Direct current
DNA	Deoxyribonucleic acid
DVT	Deep vein thrombosis
DPI	Dots per inch
FDA	Food and Drug Administration
FEA	Finite element analysis
FFMD	Flow-focusing microfluidic device
µCPC	micro Coulter particle counter
MB	Microbubble
PDMS	Polydimethylsiloxane
PTS	Post-thrombotic syndrome
RNA	Ribonucleic acid
SNR	Signal to Noise Ratio
rtPA	Recombinant tissue plasminogen activator
US	Ultrasound
UVML	University of Virginia Microfabrication Laboratory

Chapter 1. Introduction

1.1 Introduction to microbubbles

Microbubbles are gaseous bubbles that are stabilized by a lipid, protein or polymer surfactant shell with diameters frequently between 1 and 4 μm.[1,2] They are formulated to achieve a lifetime within the circulatory system on the order of approximately 10 minutes. Thus, their design requires a low solubility gas that is stabilized by a shell material (e.g. lipid monolayer) to minimize gas diffusion and prolong circulation. Microbubbles are approved by the FDA in the United States as a contrast agent for cardiac and liver imaging applications and are under investigation via clinical trials for applications in molecular imaging and therapy.[3,4]

Microbubbles exhibit a unique frequency response to acoustic excitation. Acoustic excitation causes microbubbles to oscillate at the excitation frequency due to the compressibility of the gas core. In response, acoustic energy is emitted from microbubbles at harmonic and sub-harmonic frequencies. The acoustic response of microbubbles at non-fundamental frequencies can be detected to differentiate microbubbles from soft tissue at high specificity and sensitivity.[5-7] Furthermore, the strongest response a microbubble emits occurs at its resonant frequency, which is a function of its radius and the viscoelastic properties of the shell material. Often, microbubbles have a resonance frequency between 5 and 10 MHz, which overlaps with a broad segment of diagnostic ultrasound imaging frequencies and, thus, makes them exemplary contrast imaging agents.[5]

In addition to diagnostic imaging applications, many therapeutic applications exist in which microbubbles may be beneficial. The same oscillatory behavior that benefits imaging applications can also be harnessed therapeutically. Specifically, the incident ultrasound energy on a microbubble causes rapid oscillation of the microbubble shell material that perturbs its

surrounding environment. Further, larger microbubbles exhibit greater bioeffects.[8-12] Borrelli *et al*. reported improved clot dissolution for 3 μm MBs versus 1 μm MBs.[9] Despite this finding, the diameter of the microbubble remains largely uninvestigated because groups investigating therapeutic applications of microbubbles[13-21] have been confined to intravenous MB administration with commercially available MB formulations.[22]

1.2 Introduction to microbubble fabrication techniques

Microbubbles used for diagnostic imaging applications are conventionally fabricated by two batch methods, agitation and sonication. The mixture of a gas-saturated solution containing the microbubble shell material can produce in excess of 1 billion microbubbles of a polydisperse mix (diameters between 0.5 and 10 μm). The batch production methods are compatible with imaging applications because a great number of microbubbles are required to withstand intravenous injection, while stability is necessary to complete multiple passes through the circulatory system.[23]

Alternatively, microbubbles may be fabricated in a serial manner by a microfluidic device, most commonly using flow-focusing microfluidic device (FFMD) design.[24-27] Within a microfluidic device pressurized flows of liquid and gas are conveyed through microchannels and combine with high fidelity and repetition to fabricate microbubbles.[28] Due to the highly precise and repetitive nature of the fluids, microbubbles are produced with diameters that are nearly uniform. In imaging applications, a monodisperse population of microbubbles can improve SNR of contrast-enhanced ultrasound imaging (CEUS).[29] Furthermore, microbubbles fabricated using a microfluidic device can be tuned in size and temporal stability based on the application. Thus, instead of aiming for long circulation lifetimes, microbubbles can be fabricated to achieve transient stability by using higher solubility gases and weaker surfactant

shells.[30,31]. A microbubble with such a composition profile may then be fabricated in a microfluidic device at a vascular site only to be active at the intended therapeutic target before dissolving downstream and reducing the possibility of off-target effects.[32] A core research initiative of our lab focuses on fabricating microbubbles via FFMDs that enable *in situ* MB production[30,32,33] of large, transiently stable MBs (Ø > 10 um, half-life < 45 s) specifically for therapeutic applications, such as sonothrombolysis.

1.3 Introduction to microbubbles for sonothrombolysis applications

Sonothrombolysis is the combination of ultrasound and microbubbles, with or without a thrombolytic drug (commonly rtPA), to enhance the dissolution of blood clots in patients that present with thrombo-occlusive diseases, such as acute ischemic stroke, deep vein thrombosis, and pulmonary embolism.[34-36] The first mechanism of sonothrombolysis is cavitation. Upon insonation, a microbubble that cavitates may undergo a violent collapse that chisels away the exterior and interior components of the clot.[10,37] Second, microbubbles provide mechanical disruption at the clot surface via tunneling through the fibrin mesh of the clot, which enhances rtPA transport into deeper layers of the clot and increases the number of available binding sites for rtPA to disrupt the structure of the clot.[38-43]

Sonothrombolysis was evaluated as a therapy for acute ischemic stroke in clinical trials to mixed results.[34,35,44] The investigations demonstrated that while sonothrombolysis accelerated the rate of thrombolysis versus intravenous administration of rtPA, patients experienced an elevated risk of intracranial hemorrhage. Low frequency (< 750 kHz) ultrasound in combination with rtPA increased risk of atypical hemorrhage, possibly due to the creation of standing pressure waves.[43,45] Where diagnostic (> 1 MHz) ultrasound was used, symptomatic

hemorrhage rates were similar to existing therapies.[34,35] Still, suboptimal ultrasound and microbubble protocols depress *in vivo* therapy performance.[9]

Deep vein thrombosis may be another thrombo-occlusive disease that has the potential to benefit from sonothrombolysis therapy. DVT affects approximately 0.1% of adults in the United States annually.[46,47] Standard treatment of acute DVT includes the administration of either unfractionated or low-molecular weight heparin followed by vitamin K antagonists such as warfarin (coumadin).[48] The goals of anti-coagulant therapy are to prevent the extension of the blood clot, lower the incidence of pulmonary embolism and prevent recurrence of the disease.[48,49] Approximately 25-50% of patients will experience venous dysfunction due to the insufficient recanalization of their afflicted vein and develop post-thrombotic syndrome (PTS).[49,50] An additional approach is catheter-directed thrombolysis (CDT), in which a thrombolytic drug is administered locally at the venous thrombus, is effective at lysing the thrombus; however, many patients with residual or return thrombi may develop PTS.[49,50] Sonothrombolysis may be a compatible therapy to accelerate the removal of thrombi in DVT.

1.4 Introduction to micro Coulter particle counters[1]

The Coulter counter spurred a rapid evolution in the ability to quantify and differentiate cell populations.[51,52] The Coulter Principle states that as a particle suspended in an electrolyte passes through a sensing zone (typically an orifice in the case of classical Coulter counters), the particle displaces the electrolyte within the sensing zone, giving rise to an impedance perturbation proportional to the particle volume.[53-55] The impedance perturbation is measured

[1] This section contains content from the following peer-reviewed conference and journal publications:
JMR Rickel, AJ Dixon, AL Klibanov, JA Hossack. "A flow focusing microfluidic device with an integrated micro coulter particle counter for sequential production and characterization of size tunable microbubbles". *Lab Chip*, 2018, **18**, 2653 – 2664.

by applying a potential across two electrodes near the detection region and sensing the perturbation in electrical current flow. The fields of microfabrication and microfluidics[56,57] have provided a pathway to a miniaturized Coulter counter that is now frequently referred to as micro Coulter Particle Counters (μCPC).[58-60]

Particles characterized by resistive pulse sensing include a variety of cell types, such as leukocytes and red blood cells, DNA, RNA, viruses, polystyrene beads, and oil-in-water emulsions.[61-64] Applications range across diverse fields within biomedical research from whole blood counting[65,66] to DNA sequencing through nanopores.[62]

Chapter 2. Investigation of micro Coulter particle counter geometries[2]

2.1 Introduction

Top-and-bottom electrode detection regions provide enhanced sensitivity to investigate particles;[58] however, they require fabrication equipment that is not ubiquitous. Conversely, coplanar electrodes feature two electrodes on the same substrate. From an engineering perspective this design is easier to fabricate; however, the tradeoff is a larger detection region that inherently is less sensitive.[58]

Most applications that use µCPCs investigate characteristics of solid particles that are conveyed through a microfluidic device.[61-64,67,68] Few groups use µCPCs to investigate the production of microparticles produced by a microfluidic device.[63,69-71] Design criteria are important to implementing a suitable detection region. First, the overall volume of the detection region needs to be considered. Second, the space between the electrodes and the width of individual electrodes. The overall impedance in the channel is important to obtaining a detectable impedance change. Finally, the size of the particle to be interrogated is of utmost importance to achieving suitable performance.

Conventionally, microbubble fabrication by microfluidic devices is monitored using high-speed microscopy, which limits the scalability and portability of using microbubbles produced by an FFMD to a laboratory benchtop. This thesis demonstrates the ability to fabricate an integrated FFMD-µCPC to characterize populations of microbubbles *in situ* by electrical impedance spectroscopy.

---

[2] This chapter contains content from the following peer-reviewed conference and journal publications:
JMR Rickel, AJ Dixon, AL Klibanov, JA Hossack. "A flow focusing microfluidic device with an integrated micro coulter particle counter for sequential production and characterization of size tunable microbubbles". *Lab Chip*, 2018, **18**, 2653 – 2664.

2.2 Materials and Methods

2.2.1 Finite Element Analysis

The microbubble used in this simulation was formed by creating a sphere of given diameter and using the difference feature to subtract the sphere from the simulation environment. Thus, the simulated microbubble is rigid, hollow, and does not feature a shell. A step size of 2.5 μm was used to advance the microbubble down the channel. The step size was determined to be an equitable compromise between fine spatial resolution and computational speed.

The simulated geometry featured free tetrahedral mesh elements constrained to a user-controlled setting of 'extra fine', in which the minimum element size was 0.54 μm and maximum element size was 12.6 μm. Electrodes were designed to be offset ~ 500 nm from the edges of the simulation environment to avoid internal errors and premature breakdown of the simulation caused by the minimum element size not being able to 'fill' that area. The walls of the simulation environment were all defined as insulating except for the electrodes which were identified as either the ground or terminal electrode. The study aimed to solve the following domain equations:

$$\boldsymbol{\nabla \cdot J = Q_j},$$ Equation 2.1

$$\boldsymbol{J = \sigma E + J_e},$$ Equation 2.2

$$\boldsymbol{E = -\nabla \cdot V},$$ Equation 2.3

A numerical solution was determined with an iterative solver that used conjugate gradients method to solve the differential equations. Convergence to a given tolerance of error was used as the termination technique for each step.

FEA was performed using the AC/DC module of COMSOL Multiphysics (v. 4.4, Burlington, MA). Two discrete segments of the FFMD geometry (Figure 2.1A,B) were simulated – the detection region of the expanding nozzle defined by the detection region electrodes and the straight channel of the liquid inlet defined by the reference arm electrodes. The dimensions of the detection region were 20 µm tall with a 5 µm nozzle that expanded 65° with respect to the nozzle. The reference arm dimensions were 20 µm tall, 50 µm wide and 100 µm long. All simulations used a 3 V_{pp}, 1 MHz sinusoid applied in a medium resembling 0.9% physiologic saline ($\sigma = 1.6$ S m^{-1}; $\varepsilon_r = 80$).

Three sets of simulations were designed to investigate various conditions encountered within the flow focusing microfluidic device. Simulations were designed to determine (i) the impedance magnitude at a defined frequency in the detection region and reference arm without the presence of a microbubble (Figure 2.1A,B); (ii) the impedance magnitude perturbation in the detection region caused by the passage of a single microbubble of selected diameters (Figure 2.1C) and (iii) the impedance magnitude perturbation in the detection region caused by a train of four microbubbles of various diameters and various centre-to-centre spacing (Figure 2.2D).

Simulations were performed that quantified the impedance magnitude perturbation for microbubbles of various diameters against combinations of electrode widths and spacings (Figure 2.2 and Table 2.1). The first sets of simulations were devised to match the impedance magnitude in the detection region to the impedance magnitude in the reference arm. For example, the two detection region electrodes (EL_D) were 10 µm wide and extended the width of the channel. The electrodes were spaced 15 µm apart from one another. The closest edge of the first electrode was 20 µm downstream of the nozzle. The simulation for

this design determined that the impedance magnitude is 30 kΩ in the detection region. After deriving the impedance magnitude in the detection region, a complementary electrode configuration was designed for the reference arm such that its impedance magnitude was also 30 kΩ. This electrode configuration was chosen specifically for its ability to interrogate 15 µm diameter microbubbles and for its availability to be printed on a transparent photomask (discussed below) offering 10-fold cost savings and 50-fold time savings versus a chrome-on-quartz photomask providing an efficient way to add µCPC functionality to the FFMD.

For the second set of simulations, a microbubble, modelled as a rigid, hollow sphere, was introduced and incrementally moved through the detection region (Figure 2.1C). The centre of the microbubble was positioned at the midpoint of the channel height, or z = 10 µm, and at the middle of the expanding nozzle, y = 0 µm. The microbubble was moved through the detection region and the magnitude of impedance perturbation due to the movement of the microbubble was evaluated from the results.

Finally, after simulating a single microbubble passing through the detection region, the simulation was adapted to accommodate multiple microbubbles passing in a single file line through the detection region. Centre-to-centre distance between successive microbubbles was varied to represent microbubbles generated at differing production rates.

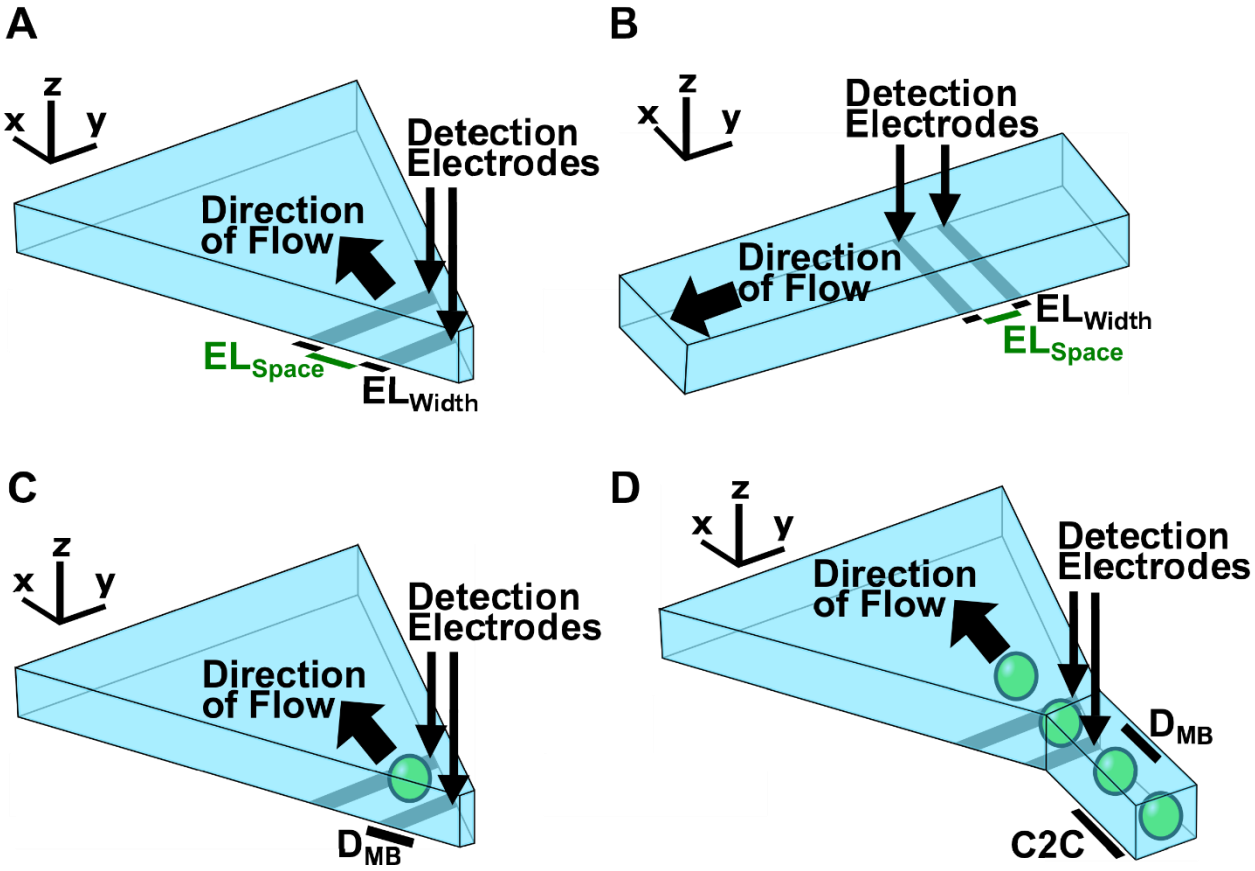

Figure 2.1 Schematic of simulations performed. A) Combinations of the variables electrode space (kerf), EL_{Space}, and electrode width, EL_{Width}, in the expanding nozzle were simulated to determine impedance in the detection region without the presence of an MB. B) Combinations of the variables electrode space (kerf), EL_{Space}, and electrode width, EL_{Width}, in the reference arm were simulated to determine impedance in the reference detection region. C) Single MB investigation was performed by varying MB diameter, D_{MB}. D) Multiple MB investigation was performed by varying MB diameter, D_{MB}, and centre-to-centre distance, C2C.

2.3 Results

2.3.1 FEA results from detection of a single microbubble

FEA provided theoretical performance of the device for a single microbubble passing through the detection region. Figure 2.3A illustrates the FEA simulation environment used to determine *in situ* impedance magnitude modulation in the detection region and was previously described in Section 2.2.1. Figure 2.3B describes the impedance magnitude modulation as a

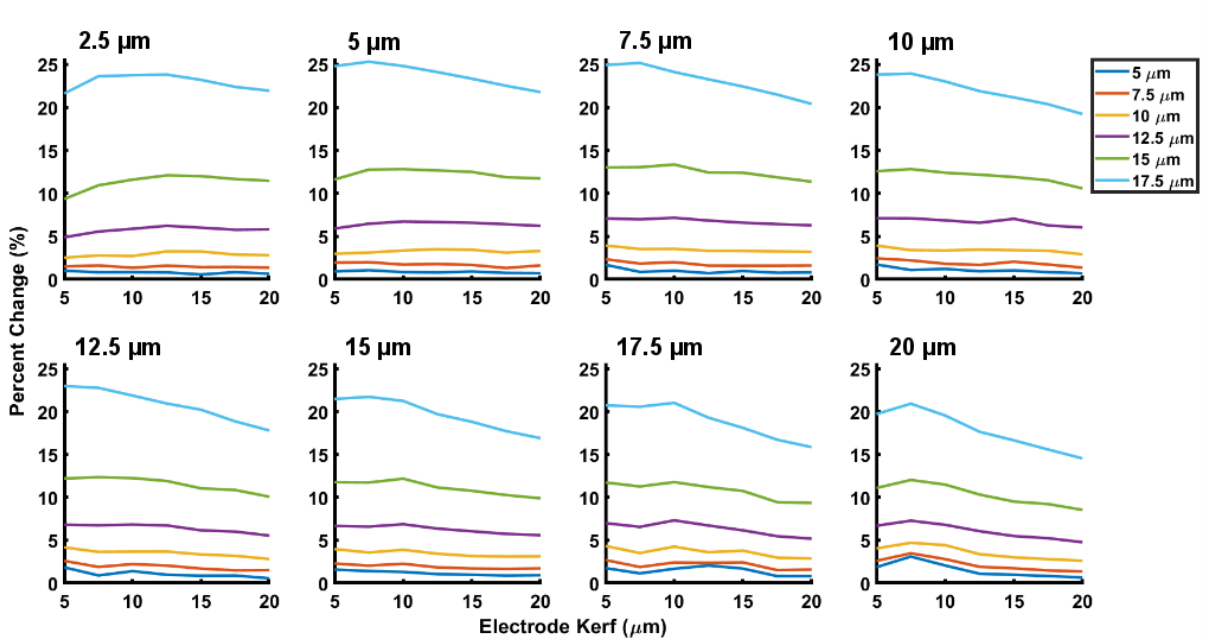

Figure 1.2 Numerical studies simulating maximum impedance perturbation for single microbubbles traversing various electrode configurations. A maximum impedance perturbation is plotted as a percent change across a range of electrode kerfs. Electrode width is provided in the upper left of each subfigure. Each curve represents a single microbubble of a given diameter (5, 7.5, 10, 12.5, 15, 17.5 µm).

function of microbubble position with respect to the nozzle. Each curve represents a microbubble of a given diameter between 7.5 and 17.5 µm incremented along the channel by 2.5 µm step sizes. The range of diameters simulated was determined by the physical constraints of the FFMD. Microbubbles larger than the height of the channel (> 20 µm) exhibit a deformed cylindrical shape and deviate from the characteristic spherical shape of microbubbles investigated in this study. Additionally, microbubbles produced in the geometrical controlled regime of the FFMD exhibited a minimum diameter of 8 µm, as determined by the nozzle width. Therefore, the study investigated the production of microbubbles between approximately 8 and 20 µm in diameter. The range of microbubble diameters investigated coincides with our intended application of improved sonothrombolysis.

The cube root of the amplitude modulation provides an estimation of microbubble diameter. Thus, the electrical diameter, D_E, is determined by the following equation:[72]

$$D_E = G_{AVG}\Delta V^{1/3}, \qquad \text{Equation 2.4}$$

Equation 1 depends on the following parameters: gain, G_{AVG} = 23.4 µm $V^{-1/3}$ (determined *in silico* for this experimental setup, see Table 2.2) and voltage modulation, ΔV_{pp}. The equation holds for the case when a single microbubble passes through the detection region without interference from adjacent microbubbles.

Table 2.1 Impedance change (%) for microbubbles across a range of diameters given different combinations of electrode width and spacing.

Impedance change (%) for MBs transiting at midheight of channel (z = 10)							
Electrode Dimensions (μm)		Microbubble Diameter (μm)					
Width	Space (kerf)	**5**	**7.5**	**10**	**12.5**	**15**	**17.5**
2.5	5	1.01	1.50	2.53	4.89	9.34	21.60
	7.5	0.83	1.62	2.79	5.56	10.93	23.61
	10	0.84	1.35	2.72	5.88	11.60	23.73
	12.5	0.81	1.60	3.25	6.23	12.09	23.80
	15	0.57	1.43	3.24	6.01	12.00	23.19
	17.5	0.84	1.45	2.88	5.77	11.66	22.37
	20	0.66	1.36	2.81	5.82	11.46	21.93
5	5	0.92	1.95	2.97	5.91	11.61	24.78
	7.5	1.07	2.00	3.12	6.47	12.76	25.30
	10	0.85	1.72	3.36	6.73	12.81	24.80
	12.5	0.80	1.79	3.51	6.66	12.66	24.09
	15	0.92	1.68	3.44	6.58	12.49	23.33
	17.5	0.75	1.32	3.12	6.41	11.87	22.50
	20	0.72	1.63	3.31	6.22	11.74	21.77
7.5	5	1.70	2.34	3.94	7.08	13.00	24.92
	7.5	0.87	1.84	3.53	6.98	13.04	25.15
	10	1.01	2.00	3.55	7.16	13.35	24.10
	12.5	0.72	1.61	3.32	6.84	12.42	23.25
	15	0.97	1.60	3.32	6.59	12.40	22.42
	17.5	0.77	1.60	3.25	6.42	11.86	21.47
	20	0.81	1.62	3.20	6.29	11.36	20.40
10	5	1.73	2.45	3.93	7.11	12.57	23.79
	7.5	1.09	2.21	3.40	7.10	12.82	23.93
	10	1.22	1.82	3.36	6.86	12.40	23.00
	12.5	0.94	1.68	3.46	6.58	12.17	21.88
	15	1.05	2.06	3.39	7.04	11.90	21.15
	17.5	0.84	1.73	3.34	6.27	11.52	20.35
	20	0.71	1.37	2.91	6.04	10.57	19.22

Table 2.1 (continued) Impedance change (%) for microbubbles across a range of diameters given different combinations of electrode width and spacing.

Impedance change (%) for MBs transiting at midheight of channel (z = 10)							
Electrode Dimensions (μm)		Microbubble Diameter (μm)					
Width	Space (kerf)	**5**	**7.5**	**10**	**12.5**	**15**	**17.5**
12.5	5	1.85	2.60	4.18	6.82	12.21	22.98
	7.5	0.90	1.89	3.64	6.75	12.35	22.77
	10	1.40	2.22	3.67	6.83	12.25	21.87
	12.5	0.98	2.05	3.68	6.73	11.91	20.94
	15	0.87	1.70	3.35	6.16	11.05	20.22
	17.5	0.89	1.49	3.19	6.01	10.86	18.86
	20	0.56	1.52	2.81	5.54	10.07	17.79
15	5	1.58	2.29	3.97	6.67	11.76	21.47
	7.5	1.41	2.04	3.57	6.59	11.73	21.72
	10	1.31	2.26	3.89	6.87	12.18	21.24
	12.5	1.06	1.84	3.43	6.36	11.15	19.70
	15	0.98	1.71	3.17	6.05	10.77	18.81
	17.5	0.89	1.67	3.10	5.74	10.27	17.72
	20	0.93	1.72	3.13	5.60	9.89	16.90
17.5	5	1.76	2.70	4.34	7.00	11.74	20.73
	7.5	1.14	1.88	3.51	6.56	11.27	20.57
	10	1.68	2.41	4.26	7.32	11.78	21.02
	12.5	2.06	2.37	3.60	6.72	11.20	19.29
	15	1.70	2.42	3.79	6.16	10.75	18.11
	17.5	0.82	1.52	2.97	5.47	9.44	16.72
	20	0.81	1.58	2.87	5.19	9.36	15.86
20	5	1.87	2.60	4.05	6.70	11.10	19.72
	7.5	3.10	3.48	4.71	7.28	12.03	20.92
	10	2.06	2.80	4.43	6.80	11.49	19.54
	12.5	1.10	1.91	3.38	6.06	10.33	17.65
	15	0.98	1.73	3.01	5.49	9.51	16.65
	17.5	0.83	1.48	2.80	5.24	9.22	15.58
	20	0.66	1.36	2.61	4.77	8.54	14.54

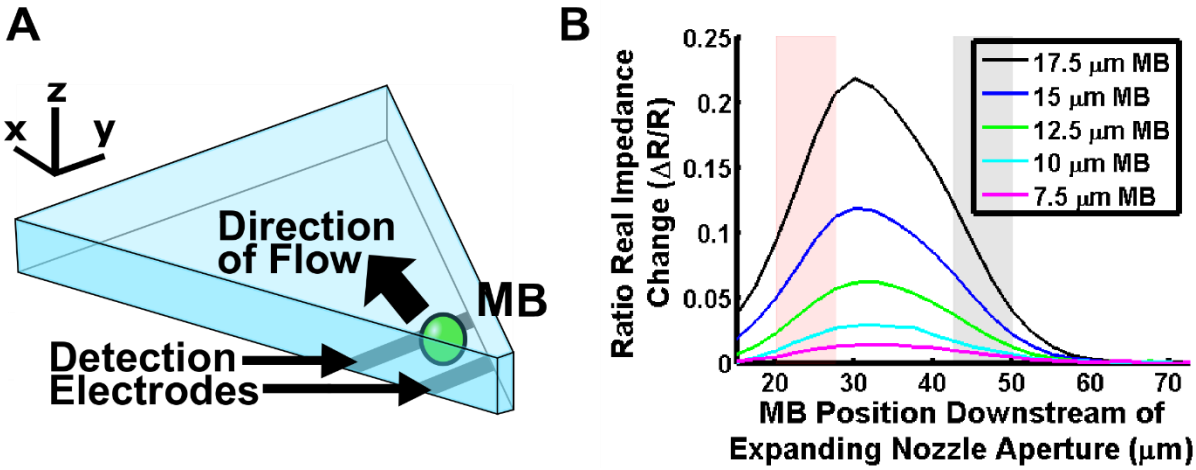

Figure 2.3 Single microbubble FEA investigation. (A) Microbubble (MB) through the expanding nozzle and passing over active and ground electrodes of a FFMD-μCPC – Modeled using COMSOL. (B) Normalized Ratio of impedance change for microbubbles of various sizes passing through the FFMD-μCPC. The red and black pairs of vertical lines denote the width and position of the active and ground electrodes in the expanding nozzle.

2.3.2 FEA results from detection of multiple microbubbles

The impedance magnitude curve for a train of four microbubbles of a given diameter and centre-to-centre spacing is presented in Figure 2.4A, in conjunction with a schematic explaining the centre-to-centre spacing variable. Figure 2.4B illustrates how the relative and absolute impedance magnitude changes as a function of spacing between consecutive 15 μm diameter microbubbles. The absolute impedance magnitude increases as consecutive 15 μm diameter microbubbles simultaneously traverse the detection region and, consequently, the signal is perceived as a larger microbubble rather than two smaller microbubbles. As shown in Figure 2.4C, the constructive interference between two microbubbles simultaneously passing through the detection region consumes greater than

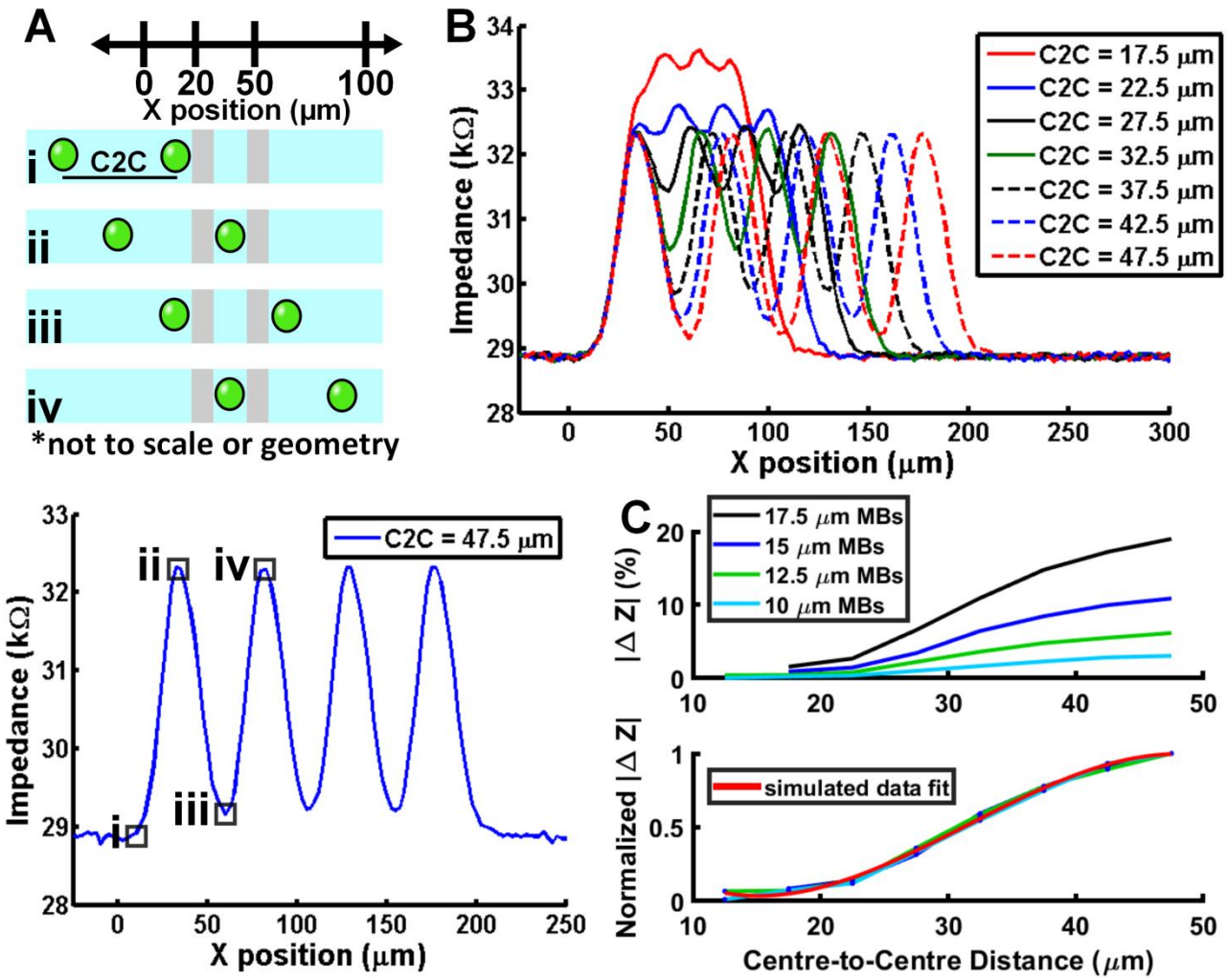

Figure 2.4 Multiple microbubble FEA investigation. (A) Top – Schematic detailing derivation of centre-to-centre (C2C) distance between microbubbles. Bottom – representative result of 15 µm microbubbles with 47.5 µm centre-to-centre spacing between each microbubble. (B) Simulation results from multiple microbubbles of a given diameter passing over the electrodes highlight the signal dependence on centre-to-centre spacing between microbubbles. (C) Top – Simulation results indicating the impact of microbubble centre-to-centre spacing for different diameter microbubbles. Bottom – Normalized curve depicting the simulated data follows a cubic relationship.

90% of the sensors dynamic range as the centre-to-centre spacing approaches the diameter of the microbubbles.

2.3.3 FEA model to correct for centre-to-centre distance dependant impedance change

During instances of microbubbles impinging on one another's electrical signal, the relative change in measured impedance magnitude attributable to each individual

microbubble is attenuated, and the formula for determining electrical diameter in the case of a single microbubble is no longer valid (Equation 2.4)). However, as shown in Figure 2.4C, when the relative impedance magnitude curves for each microbubble diameter are normalized to their maximum value, a cubic relationship exists (red curve) between the relative scaling effect and the centre-to-centre distance (R^2 = 0.99). Critically, the scaling effect is independent of microbubble diameter, which means Equation 2.4 can be modified by a scaling correction factor that accounts for the constructive interference caused by the presence of multiple microbubbles within the detection region. Thus, a corrected electrical diameter may be determined by the following equation:

$$D_{E,corected} = CF(x)G_{AVG}\Delta V^{1/3}, \quad \text{Equation 2.5}$$

where $CF(x)$, the corrective term, is a function of x, the centre-to-centre spacing, and is derived from a linear regression of curvilinear data relating the normalized impedance magnitude to the centre-to-centre distance between microbubbles, as shown by the red curve in Fig. 2.4C. $CF(x)$ takes the form of,

$$CF(x) = c_1x^3 + c_2x^2 + c_3x + c_4, \quad \text{Equation 2.6}$$

where values for c_1, c_2, c_3, and c_4 can be found in Table 2.2 and fit the simulated curves in Figure 2.4C. Values of $C(x)$range between 1 and 20 (unitless) and are valid for production rates between 0 and 3.25 x 10^5 MB s^{-1} as determined empirically. The correction factor and compensation method presented in this work is analogous to a compensation method correcting for the positional dependence of particles traversing a channel with coplanar electrodes proposed by Errico *et al.*[72] This regression will be described in the 'calibration method' section of the methods (denoted as '2.' in Figure 3.3) and will be further characterized in section 3.3.4.

Table 2.2 Values of coefficients that determine the curves produced by Equations 2.6 and 3.1. The curve in the top subplot of Figure 2.4C uses the 10 – 17.5 μm microbubble (MB) coefficients. The curves in the bottom subplot of Figure 2.4C and Figure 3.7B use the normalized value 'c' coefficients. The surface plot of Figure 3.7A uses the 'b' coefficients.

	c_1	c_2	c_3	c_4
10 μm MB	-1.498×10^{-4}	1.428×10^{-2}	-0.3208	2.149
12.5 μm MB	-3.487×10^{-4}	3.283×10^{-2}	-0.7598	5.463
15 μm MB	-7.965×10^{-4}	7.649×10^{-2}	-1.938	15.58
17.5 μm MB	-1.184×10^{-3}	0.1132	-2.755	21.30
normalized value	-5.437×10^{-5}	5.144×10^{-3}	-0.1183	0.8366
	b_1	b_2	b_3	b_4
value	33.224	-1.1904×10^{-4}	-7.4976×10^{-2}	6.223×10^{-12}

2.4 Discussion

A limitation of the FEA simulations is that a constant spacing is maintained between the microbubbles as they flow through the expanding nozzle, which does not account for the reduction in speed out of the nozzle of microbubble approximately 40-50 μm downstream of the nozzle. The observed decrease in velocity by the microbubble occurs while it is within the detection region, specifically over the ground electrode, and thus still imposes and consequently interferes with the modulated electrical signal detected. It is possible to mitigate this effect by shortening the width of the coplanar electrodes, thereby decreasing the length of the detection region. Interestingly, simulation results predict detection does not improve by an appreciable amount due to the change in coplanar channel geometry; however, the pulse width does narrow as expected. One would expect an enhanced ability to distinguish production rates $< 3.25 \times 10^5$ MB s^{-1} and, consequently, a decreased dependence on applying a production rate correction factor.

2.5 Conclusions

Simulations informed the design of the electrode detection region and established the theoretical performance of the FFMD-μCPC device. Single microbubble simulations established the maximum impedance magnitude modulation within the detection region. Multi-microbubble simulations established the anticipated impedance magnitude modulation for microbubbles of a given diameter at variable production rates and established a relationship to relate the simulated centre-to-centre distance between successively produced microbubbles to a correction factor. Further, a finite element analysis model was developed to be one component of a calibration method that accounted for the interference resulting from the presence of multiple microbubbles in the detection region simultaneously.

Chapter 3. Development of a benchtop flow focusing microfluidic device with integrated electrical characterization of monodisperse microbubbles[3]

3.1 Introduction

μCPCs enable the analysis and size measurement of single particles of interest in a lab-on-a-chip environment using electrical or optical methods of measurement.[67,68] Optical methods incorporate waveguides and optical fibers to detect light-scattering or light-blocking during the passage of a particle through the detection region.[73,74] Methods of electrical interrogation of particles and cells include impedance-based approaches using DC or AC excitation to measure volume.[58,75,76] Capacitive sensors have been employed to measure two-phase flow in microfluidic devices.[77,78] The resistive pulse sensor is the dominant practical approach.[53,61,79]

Many impedance-based spectroscopic devices have developed diverse methods to enhance particle sensing by electrode configuration,[58,80] hydrodynamic focusing,[58,59,66,81,82] physical noise reduction techniques[83,84] and signal processing.[85-87] Innovation has also occurred with respect to enhancing throughput of the devices by utilizing multiple apertures[60,88] and radiofrequency transmission.[89] Reasons for relatively low throughput include the need for dilute suspensions of particles for individual detection through micron-dimensioned channel constrictions to avoid coincident particle detection and device clogging. However, pressure-driven flow allowed Fraiken *et al*. to achieve detection of > 5 x 10^5 nanoparticles s^{-1} through a nanopore constriction.[90]

[3] This chapter contains content from the following peer-reviewed conference and journal publications:

JMR Rickel, AJ Dixon, AL Klibanov, JA Hossack. "A flow focusing microfluidic device with an integrated micro coulter particle counter for sequential production and characterization of size tunable microbubbles". *Lab Chip*, 2018, **18**, 2653 – 2664.

JMR Rickel, AJ Dixon, AL Klibanov, JA Hossack. "A flow focusing microfluidic device with an integrated micro coulter particle counter for sequential production and characterization of size tunable microbubbles." IEEE International Ultrasonics Symposium (2017), Washington, DC, USA.

Driven by application-specific requirements, most μCPCs process particles from off-chip sources (e.g. blood), convey them into an inlet, through the detection region, and out of the device. However, μCPCs have also been applied to the detection of particles produced *in situ* (i.e. on-chip), such as droplets and air-slugs produced by the controlled mixing of two-phase microfluidic flows.[63,69] Niu *et al*. demonstrated by capacitive sensing the detection and sorting of 50 μm aqueous droplets produced by a T-junction.[63] Additionally, capacitive sensing using interdigital electrode geometry has been demonstrated for the detection of 900 μm water-in-oil emulsions produced by flow focusing.[71] Yakdi *et al*. reported detecting and sizing oil droplets greater than 50 μm in diameter generated by a T-junction by measuring impedance fluctuations.[70]

Further improvements in μCPC throughput and detection sensitivity are required to sense smaller particles produced *in situ,* especially microbubbles and microdroplets with diameters less than 20 μm produced at rates often exceeding 1×10^5 particles / s.[24,28,91] Microbubbles with diameters between 1 – 20 μm, in particular, have broad utility in biomedical engineering. Notable applications include their use as diagnostic ultrasound imaging contrast agents to enhance echocardiograms[71,92] and as therapeutic agents for gas embolotherapy,[93,94] localized drug and gene delivery via sonoporation,[95,-97] and accelerated dissolution of thrombus to promote revascularization in ischemic stroke.[34,35,91,98] Microbubbles are most commonly produced in large, polydisperse batches via either sonication or agitation;[99-100] however, they can be fabricated in monodisperse populations using a variety of microfluidic device designs. These designs include: T-junction,[28] co-flow[101] and flow-focusing.[24-27] Microbubbles produced by microfluidic devices have the advantage of being tunable in terms of size and temporal stability.[8,24-27,102] Conventionally,

microbubble fabrication by microfluidic devices is monitored using high-speed microscopy, unfortunately limiting the scalability and portability of the technique. In this work, we demonstrate the ability to fabricate a FFMD with integrated μCPC (FFMD-μCPC, Figure 3.1) functionality to characterize populations of microbubbles immediately after production by electrical impedance spectroscopy. Simulations informed the design of the integrated electrode detection region, established the theoretical performance of the device, and were validated by experimental data.

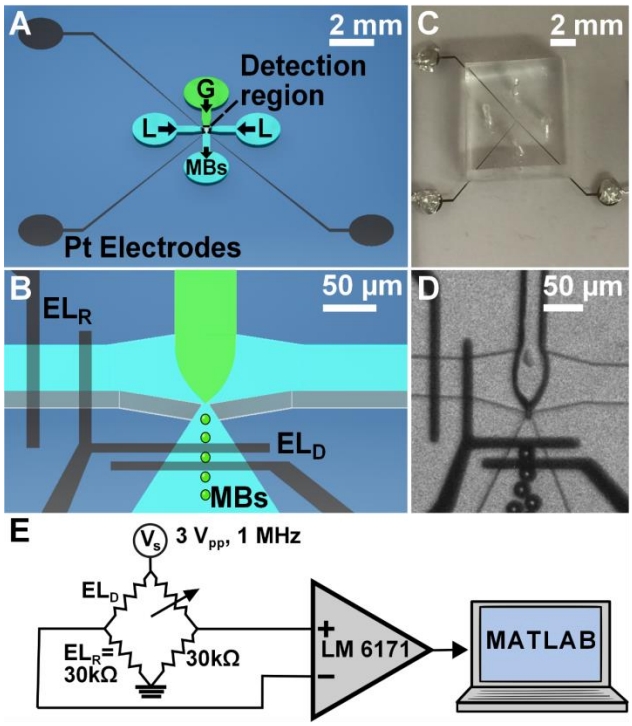

Figure 3.1 (A) Schematic of Benchtop FFMD-µCPC. G = Nitrogen Gas, L = Liquid Phase, MBs = Microbubbles. (B) Three-dimensional view of FFMD-µCPC with blown up nozzle where microbubbles are produced and traverse electrodes. EL_R = Continuous Phase Channel Reference Electrodes, EL_D = Expanding Nozzle Detection Region Electrodes. (C) Image of Benchtop FFMD-µCPC. (D) Benchtop FFMD-µCPC producing 15 µm microbubbles under 20x magnification. (E) Schematic of electrical detection circuit.

3.2 Materials and Methods

3.2.1 Device Fabrication

The microfluidic device consisted of two pairs of coplanar electrodes integrated within a flow focusing microfluidic device. A schematic detailing the fabrication steps is provided as Figure 3.2. The electrodes were fabricated using standard microfabrication lift-off techniques.[8,32,58,60,91,102] Bi-layer photolithography, using positive photoresists LOR10B and AZ4110 (MicroChem, Newton, MA), was performed to pattern the electrode design on a glass wafer. For this photolithographic procedure, a transparent photomask (CAD Art/Services, Inc, Bend, OR) at 20,000 DPI was used. Electron beam evaporation deposited

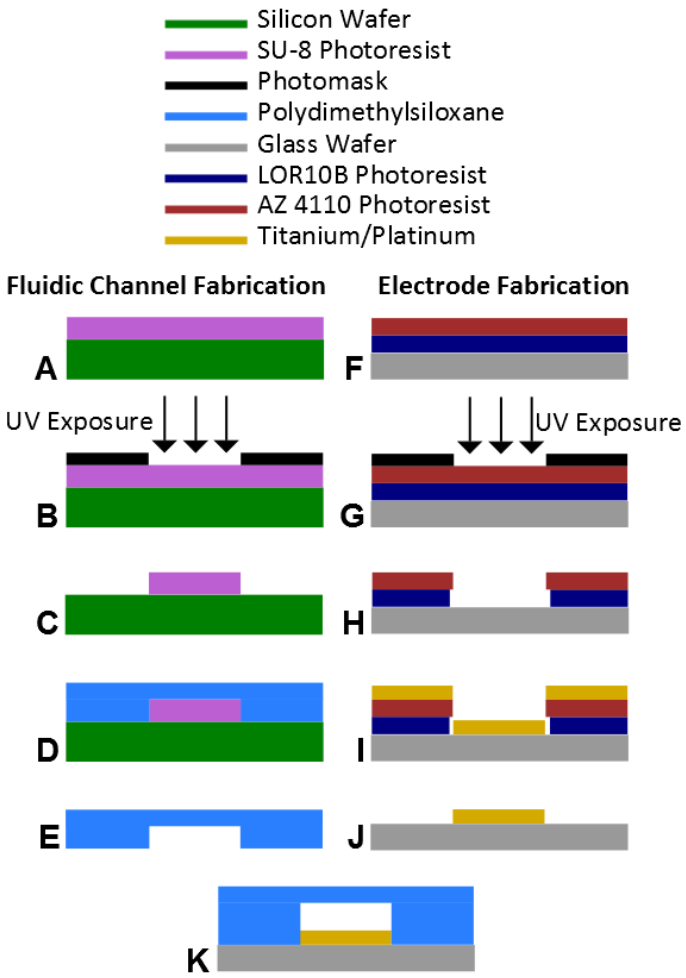

Figure 3.2 Microfabrication techniques used to fabricate the FFMD-µCPC. The fluidic channels are formed by (A) applying a negative photoresist, SU-8 3025, to a silicon wafer and (B,C) performing photolithography. Subsequently, (D,E) soft lithography is performed using PDMS. The electrodes are constructed by (F) applying positive photoresists LOR 10B and AZ 4110 sequentially to a glass wafer, followed by (G,H) photolithography, (I) electron beam evaporation and (J) bi-layer lift off. The PDMS mold containing the fluidic channels (E) is then aligned to the electrodes contained on the glass wafer and they are (K) bonded to create the end device.

20 nm Titanium (Ti) / 100 nm Platinum (Pt) on the substrate. Finally, bi-layer lift-off was performed to remove extraneous metal from the substrate.

Separately, microfluidic channel fabrication consisted of photolithography using SU-8 3025 (MicroChem, Newton, MA) to develop 20 µm tall microfluidic channels on a silicon wafer and soft lithography to cast the microfluidic channels in polydimethylsiloxane (PDMS) (Sylgard 184, Dow Corning, Midland, MI). For this procedure, a chrome on quartz

photomask (Applied Image, Inc., Rochester, NY; spot size = 0.1 μm) was used to transfer the FFMD pattern to the substrate. Together, these processes yielded the two components that form the device.

The two components were then loaded onto a custom 3D micro positioner (Thorlabs, Inc., Newton, NJ) for alignment. The micro positioner was held in a custom 3D printed adapter placed on an IX 51 microscope stage (Olympus, Center Valley, PA). The PDMS microfluidic channels were precisely aligned to the electrodes on the glass wafer using the aforementioned microscope supported with micro-manager software v. 1.4 and ImageJ. After alignment, the micro positioner was placed in an oxygen plasma oven for 30 seconds at 150 W (PE-50, Plasma Etch, Carson City, NV) to activate the PDMS surface and facilitate a bond to glass.

3.2.2 Microbubble production

Microbubble production using a FFMD has been achieved previously in our laboratory.[8,32,91,102] The microfluidic device is illustrated schematically in Figure 3.1A,B. There are two inlets through which the continuous phase enters the device. The continuous phase is 3% (weight/volume) bovine serum albumin dissolved in a solution of isotonic saline (0.9% NaCl). A third input exists through which the dispersed phase, 99.9998% purified nitrogen gas (GTS Welco, Richmond, VA), enters the system. The aperture of the expanding nozzle (5 μm wide on mask, 8 μm wide after photolithography) creates a flow constriction of the gas and liquid that causes a high shear zone due to a high velocity gradient and enables the gas cone pinch off and microbubble creation. The output orifice allows microbubbles to exit the device directly. The continuous phase was controlled by a syringe pump (PHD2000, Harvard Apparatus, Holliston, MA) and ranged between 10 – 30

µl / min during experimentation. The dispersed phase was controlled by a two-stage pressure regulator (VTS 450D, Victor Technologies International, Inc., St. Louis, MO). Gas pressure was verified at the inlet to the device using a digital manometer (06-664-21 Fisher Scientific, Pittsburgh, PA) and ranged between 40 – 100 kPa during experimentation. After each manipulation of gas pressure and liquid flow rate the device was allowed time to equilibrate.

3.2.3 Electrical Detection

The electrical detection circuit was comprised of two stages – a Wheatstone bridge and a differential amplifier (Figure 3.1E). One branch of the Wheatstone bridge included the electrodes in the expanding nozzle and the reference continuous phase channel. The other branch was comprised of a potentiometer and a 30 kΩ resistor to match the ratio of impedance magnitudes of the former branch such that the Wheatstone bridge was manually balanced prior to differential signal amplification. Differential amplification was achieved using a LM6171 (Texas Instruments, Dallas, Texas) operational amplifier with 4-fold gain. Wires were connected from the electrical detection circuit to the electrode pads on the FFMD-µCPC using silver epoxy (Parker Chomerics, Woburn, MA). A 3 V_{pp}, 1 MHz sinusoid waveform was used to excite the circuit. Microbubbles were produced by the device using the technique described in the 'Microbubble production' section and an amplitude modulated signal was acquired on GageScope (DynamicSignals LLC, Lockport, IL) software on a standalone computer and post-processed using a custom MATLAB (Mathworks, Natick, MA) script. The MATLAB script used a peak detection algorithm, based on the Hilbert transform, to evaluate the magnitude of voltage change of each

microbubble pulse as well as the number of pulses during an acquisition, which was subsequently converted to a microbubble production rate.

3.3.4 Compensation Method

A well-known limitation of micro coulter particles counters is the inability to detect two or more particles simultaneously present in a detection region because the systems are not capable of discriminating between distinct particle volumes. However, in our application, the production of microbubbles in a regular, repeating pattern near the FFMD nozzle afforded the opportunity to devise a compensation method to account for the presence of multiple microbubbles within the sensing zone.

An experimental flow diagram, Figure 3.3, describes the salient elements that comprise the compensation method. First, (denoted as '1.' in Figure 3.3) raw empirical data were acquired and a three-dimensional plot of the data revealed a relationship between two explanatory variables, fluid flow rate (FFR) and electrically determined production rate (PR), and the predictor variable, optically determined centre-to-centre (C2C) distance. Second, (denoted as '2.' in Figure 3.3) FEA simulations demonstrated attenuation in the impedance magnitude perturbation caused by a microbubble as a function of the distance between sequentially produced microbubbles. Importantly, a correction factor was developed to compensate for the attenuation. The correction factor is applied to a modified equation (denoted as '3.' In Figure 3.3) that describes the diameter of a microbubble as a function of the voltage perturbation caused by that microbubble in the detection region. Assuming a robust manufacturing protocol including high fidelity alignment during the assembly of devices it is envisioned that only a single calibration would be necessary per batch. However, a calibration is required each time the geometry of the detection region is

changed or altered appreciably. As a final validation of the compensation method: data were acquired through normal operation of the device, the data were post-processed using the compensation method to compare the accuracy of the developed electrical determination of microbubble diameter to the gold-standard optical microscopy method. An in-depth analysis of each element that comprises the compensation method follows.

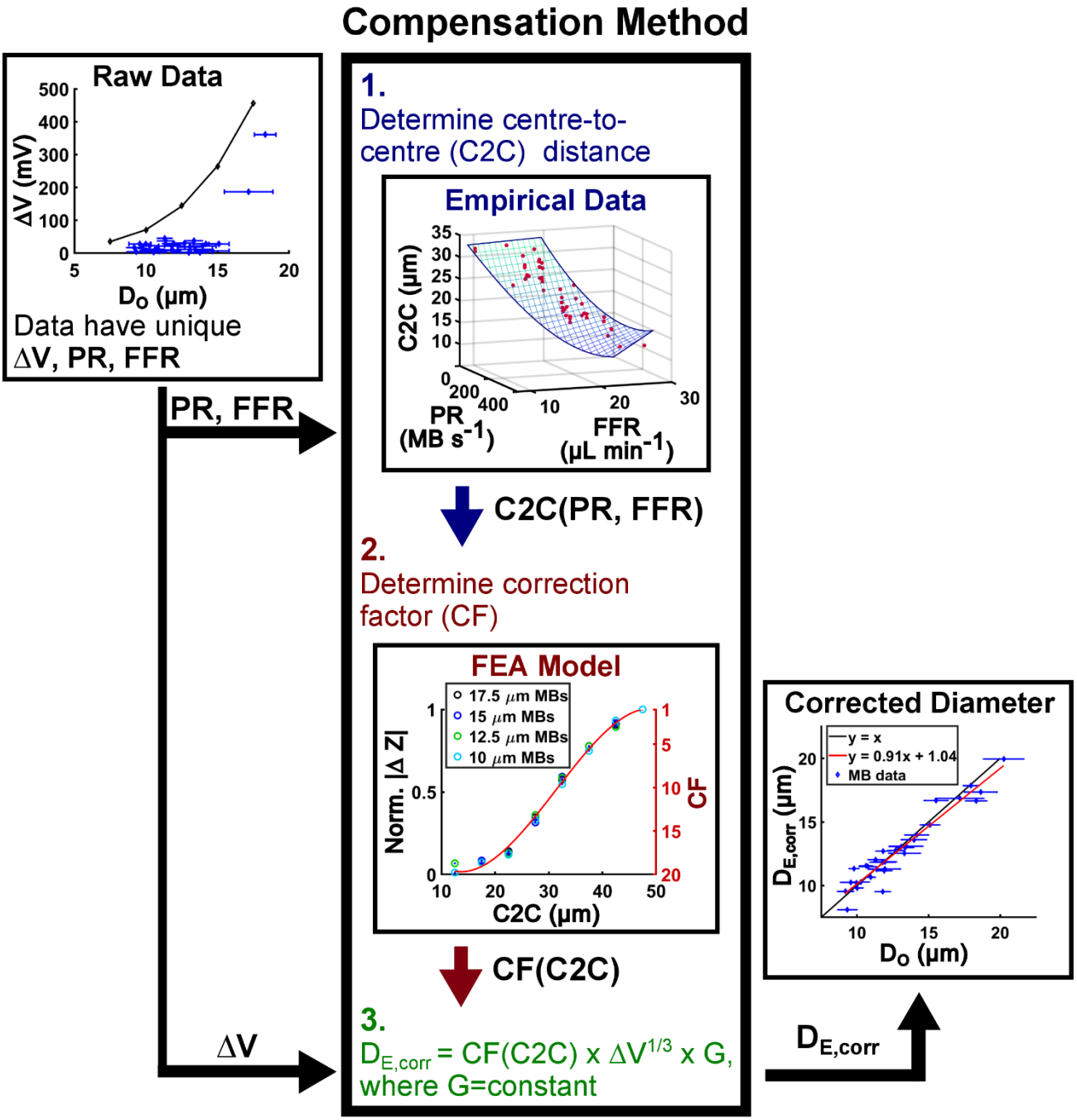

Figure 3.3 The proposed compensation method features three steps: (1) Determine the empirical relationship between the fluid flow rate (FFR; µL min^{-1}) and production rate (PR; MB s^{-1}) that yields a centre-to-centre distance (C2C; µm). (2) Determine the relationship between centre-to-centre distance and the normalized magnitude of the impedance perturbation (ΔZ; unitless) that yields a correction factor (CF; unitless). (3) Multiply the correction factor by cube root of the voltage change (ΔV; mV) and the electronic circuit gain (G; µm $V^{-1/3}$) to arrive at a corrected electrical diameter ($D_{E,\,corr}$; µm). Data are collected (upper left) and processed through the compensation method to yield a corrected electrical diameter that closely approximates the gold standard optical diameter (bottom right).

3.3 Results

3.3.1 Single microbubble experimental results

A single microbubble traversing the detection region is presented in Figure 3.4. Images acquired with a high-speed camera depict the position of a microbubble as it passed through the detection region, framed by the platinum electrodes. The first image of a series of 24 images triggers the acquisition of electrical data. Each image was synchronized with recorded electrical data to within tens of nanoseconds. Thus, each image taken of a MB provides a corresponding position along the amplitude modulated curve. The response from a single microbubble passing through the detection region is characterized by an asymmetric envelope in which the rise time is faster than its decay, as confirmed by FEA results. The shape of the envelope is explained by the asymmetric geometry of the expanding nozzle (resulting in rapid microbubble deceleration through the sensing zone) and non-uniform current density. Since the expanding nozzle has an asymmetric shape referenced by the position in the middle of the detection region, the electrode closest to the nozzle has a smaller exposed region than the electrode farthest from the nozzle. Thus, the current density, and consequent impedance change, is higher at the electrode nearest to the expanding nozzle because it has a smaller region exposed to solution, whereas the downstream electrode has a larger region exposed to the channel, resulting in lower current density.

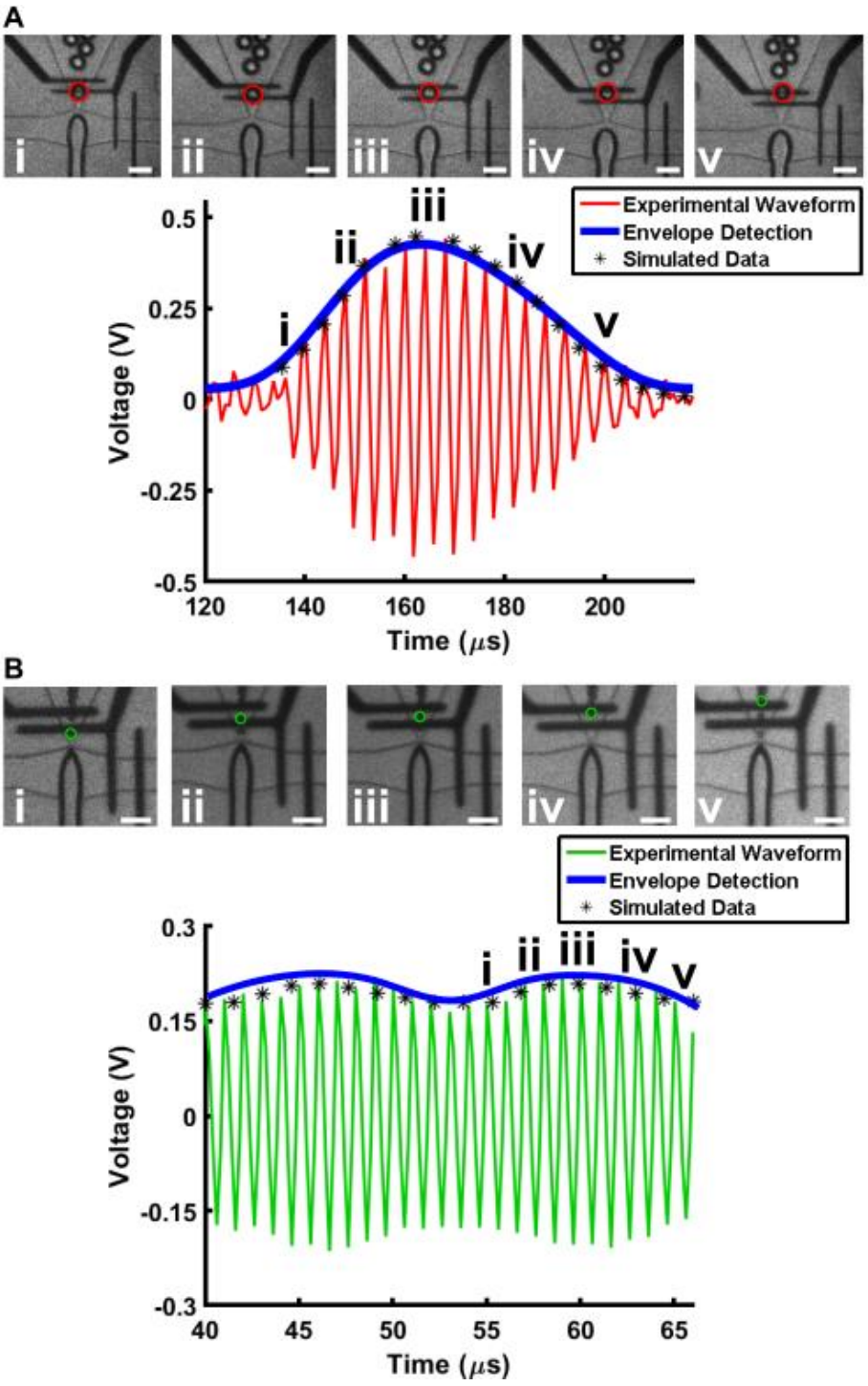

Figure 3.4 Raw voltage modulated signals. (A) A 35 µm diameter microbubble produced at 16,500 MB s^{-1}. A 35 µm microbubble is depicted for illustrative purposes but is outside the intended scope of this study. (B) A 15 µm diameter microbubble produced at 70,000 MB s^{-1}. i, ii, iii, iv, and v within the amplitude modulated signal correspond to the microbubble's position over the electrodes shown in the respective thumbnail images. Scales bars = 50 µm.

The baseline waveform when no microbubbles were produced had a standard deviation in the modulation of the waveform of 6.6 mV. The theoretical limit of detection for a single microbubble was determined to have a diameter of 2.5 μm by fitting a nonlinear regression to the impedance magnitude modulated data attained from FEA. The 7.5 μm diameter microbubble, the smallest microbubble produced by our FFMD, resulted in a signal to noise ratio of 14.6 dB.

3.3.2 Counting microbubbles

The conventional approach for establishing production rates of microbubbles produced by microfluidic devices involves measuring the time elapsed between sequential microbubble break off events as observed using high speed microscopy.[24,25,26,101] Determining microbubble production rates using this approach is tedious, typically lacks fine resolution and is susceptible to temporal sampling artifacts (e.g. aliasing). Using the electrical detection strategy presented, if each electrical voltage perturbation is distinguishable, then the production rate can be established with greater ease, accuracy and confidence. In our studies, data of captured production rates were corroborated with optically determined production rates. The optically determined production rates are compared to the electrically determined production rates ($R^2 = 0.98$) in Figure 3.5A. The residuals are plotted in Figure 3.5B. So long as the impedance magnitude perturbations give rise to signals distinguishable from the electrical noise floor, the electrically determined rate is considered to be fault-free and consistent with the decades of experience with Coulter counters which have long been considered the "gold standard" for this measurement. None of the FFMDs that we tested produced microbubbles too small to be counted reliably.

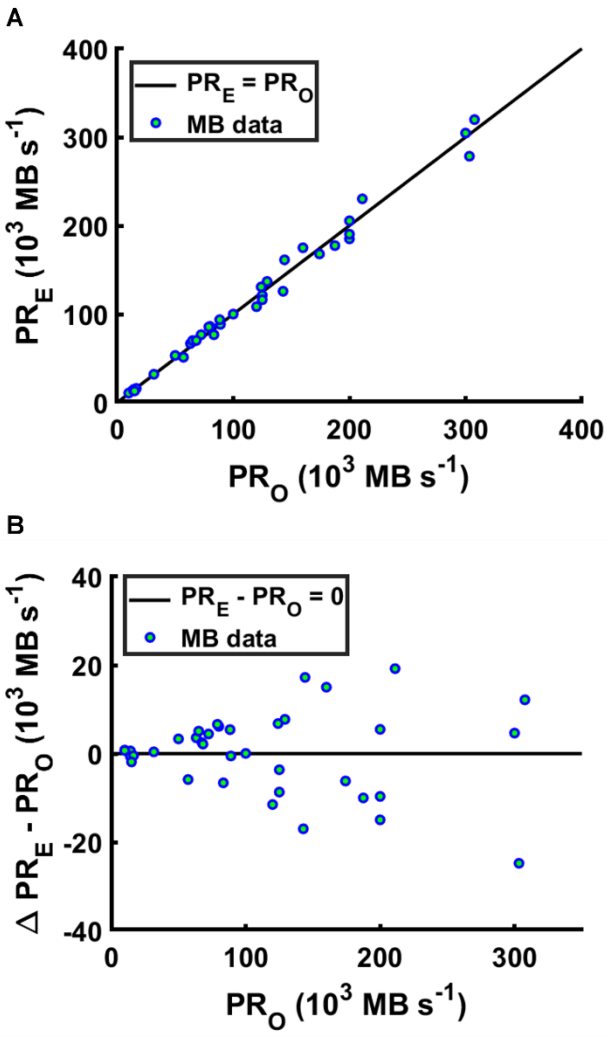

Figure 3.5 Plots showing the optical production rate (PR_O) versus the electrical production rate (PR_E). (A) Comparison of methods to determine production rate. Optically determined production rate spans the x axis and electrically determined production rates the y axis. The black line is y=x and data points on that line demonstrate excellent agreement. (B) Residuals of the production rates are plotted.

However, in rare faulty operation conditions,[102] it is possible to observe pairings of large and small bubbles. In these cases, the small bubbles will probably not be detectable. Practically, the parameters necessary to observe fault conditions are significantly different than the parameters required for normal operation such that most fault conditions characterized by significant instability are irrelevant.

3.3.3 Multiple microbubble experimental results

The FFMD was operated at varying gas pressures and liquid flow rates required to produce microbubbles of 10, 12.5, 15, and 17.5 μm diameters at different production rates. Figure 3.6 illustrates how the voltage modulation for a given microbubble diameter changes as a function of the centre-to-centre distance between successively produced microbubbles. In Figure 3.6, each circular datum point represents the average measured voltage modulation for a train of microbubbles as a function of the optically determined centre-to-centre distance within the train. Note that each datum point represents a distinct set of gas and liquid operating parameters for the device and that experimental data was taken such that measured diameters were within ±0.5 μm of the stated diameter. The experimental results qualitatively agree with the FEA simulations discussed in section 2.3.2, in that the relative modulation in voltage is significantly attenuated at production rates in which the distance between successively produced microbubbles is less than the end-to-end distance of the detection region. The majority of device operation occurs in this regime, at production rates greater than approximately 1×10^4 MB s^{-1}. Below that production rate, microbubble production tends to be characterized by doublet or triplet production that this device is currently not equipped to handle.

To quantitatively compare the experimental results to the FEA simulations, the FEA simulations were extended to include PSpice circuit simulations that evaluated the magnitude of the voltage modulation for microbubbles passing through the detection region using the amplification electronics incorporated within the experimental system. Results from the FEA simulations were used as input parameters. The solid curves in Figure 3.6 are simulated results representing the magnitude of voltage modulation for microbubbles

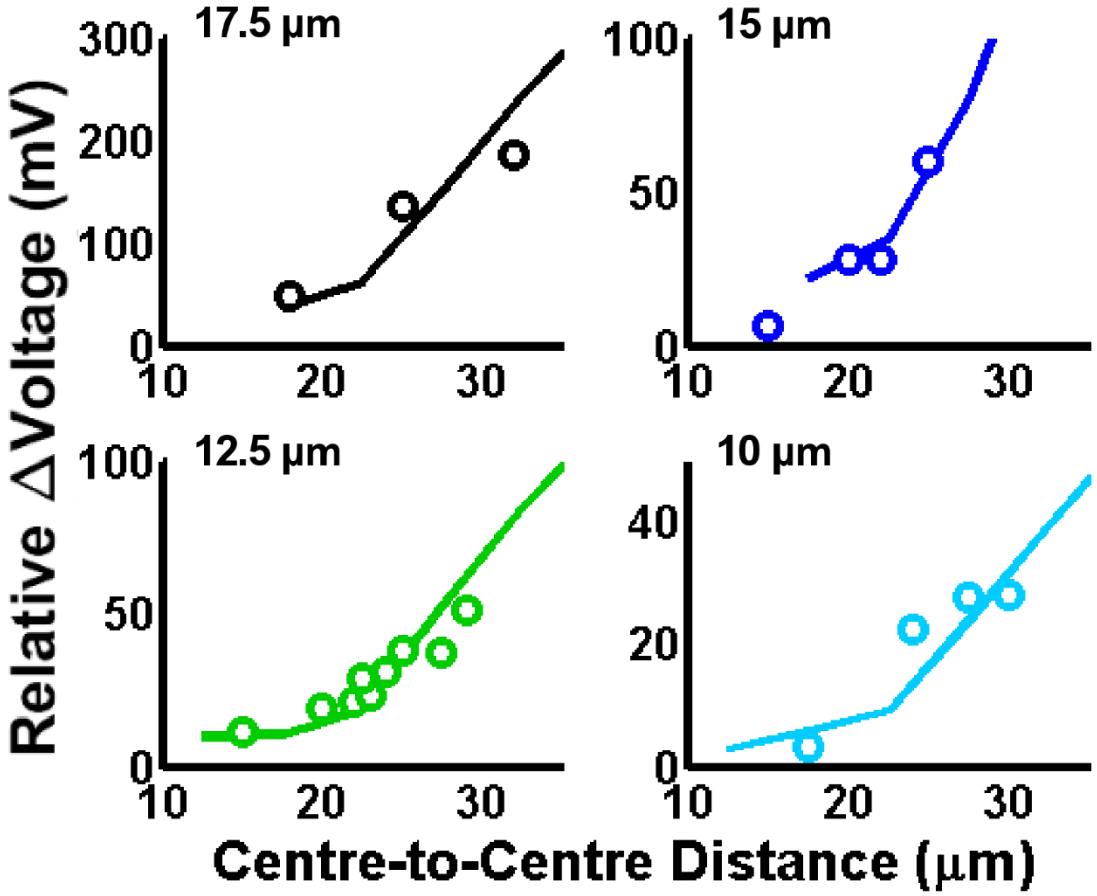

Figure 3.6 FEA simulations (solid lines) with overlaid experimental observations (open circles) of voltage modulation with varying centre-to-centre distances for (Top Left) 17.5 µm microbubbles, (Top Right) 15 µm microbubbles, (Bottom Left) 12.5 µm microbubbles and (Bottom Right) 10 µm microbubbles.

of a given diameter as a function of the centre-to-centre distance between sequentially produced microbubbles. As shown, empirically measured electrical estimates of 17.5, 15, 12.5 and 10 µm diameter microbubbles produced at varying production rates match the FEA generated curves for each optically measured microbubble diameter to coefficients of determination, (R^2 = 0.954, 0.911, 0.907 and 0.773, respectively (Figure 3.6)).

3.3.4 Compensation method

To accurately size microbubbles when more than one is located within the sensing region, the corrective scaling factor, $CF(x)$, described in 3.3.4 must be determined from the

electrically measured voltage traces. For a given set of operating conditions, $CF(x)$ of Equation 2.5 is determined through a two-step process.

First, the production rate is measured from the electrical signal using a peak detection algorithm. The electrically derived production rate (PR) and the fluid flow rate (FFR) are then mapped to a corresponding centre-to-centre (C2C) distance by the three-dimensional surface fit, as shown in Figure 3.7A. As expected, the centre-to-centre distance decreases as the production rate increases. Asymptotic behaviour is observed near a centre-to-centre distance of 10 μm as the production rate increases beyond 2 x 10^5 MB s^{-1}. This behaviour accounts for the physically limiting case that two sequential microbubbles cannot have a centre-to-centre distance smaller than their diameter. A multiple linear regression (mesh surface) was fitted to the data and to establish the relationship between the centre-

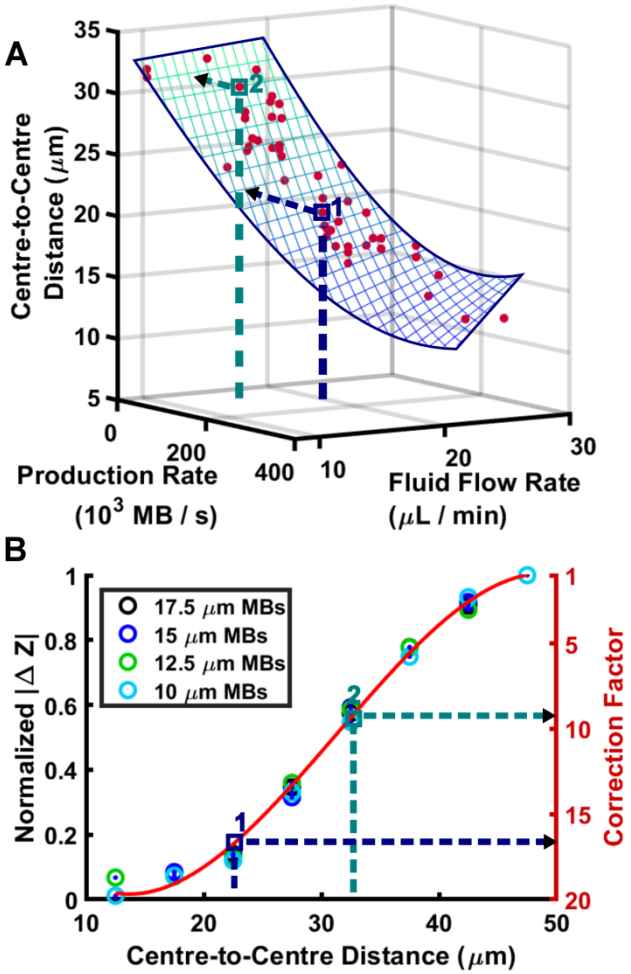

Figure 3.7 Description of the compensation strategy. (i) First, the production rate is taken from electrically acquired data and is applied to a cubic polynomial equation that relates production rate to centre-to-centre distance between microbubbles. (ii) After a centre-to-centre distance is derived, the value is used to calculate the correction factor to be applied using a cubic polynomial relationship between the centre-to-centre distance and correction factor. 10 µm and 12.5 µm microbubble data include centre-to-centre distances between 12.5 µm and 47.5 µm at 5 µm increments. 15 µm and 17.5 µm microbubble data include centre-to-centre distances between 17.5 µm and 47.5 µm at 5 µm increments.

to-centre distance, electrically measured production rate and fluid flow rate. The equation takes the form,

$$C2C(PR, FFR) = b_1 + b_2 PR + b_3 FFR + b_4 PR^2 FFR \quad , \qquad \text{Equation 3.1}$$

where values of b_1, b_2, b_3 and b_4 can be found in Table 2.2. This regression is used in the device calibration method, described in 3.3.4. The coefficient of determination for this fit was $R^2 = 0.92$.

Second, this estimate of the centre-to-centre distance is then mapped to $CF(x)$ using the red curve-fit in Figure 3.7B, which relates $CF(x)$ to the centre-to-centre distance using FEA simulated data. Equation 2.6 becomes,

$$CF(C2C) = c_1 C2C^3 + c_2 C2C^2 + c_3 C2C + c_4, \quad \text{Equation 3.2}$$

Note that the first step of this calibration process is device-specific, as the relationship between production rate and centre-to-centre distance is based on empirically measured data for a single device. We envisage that in a tight, quality-controlled, production setting, the calibration results will be generalizable over the device population. The second step is generalizable to all devices of a particular sensing geometry because it is determined from FEA simulations.

This calibration strategy was used to account for the reduced voltage modulation as multiple microbubbles passed through the sensing region. The black curve in Figure 3.8A shows the expected voltage modulation for single microbubbles of varying diameters passing through the sensing region, as simulated by the combined FEA and PSpice model. The blue data points are empirically measured voltage modulations from microbubbles passing through the sensing region and their accompanying optically-determined diameters. Prior to calibration, there exists a significant error between the expected voltage modulation (Equation 2.4) and the experimentally determined voltage modulation. However, when the experimental data were corrected for the centre-to-centre distance between successively produced microbubbles, inversely the production rate, the microbubble data tightly follows a cubic approximation as depicted in Figure 3.8B. The application of $CF(x)$ in Equation 2.5 describes the attenuation phenomenon and corrects the observed voltage modulation for scaling related to reduced centre-to-centre distances.

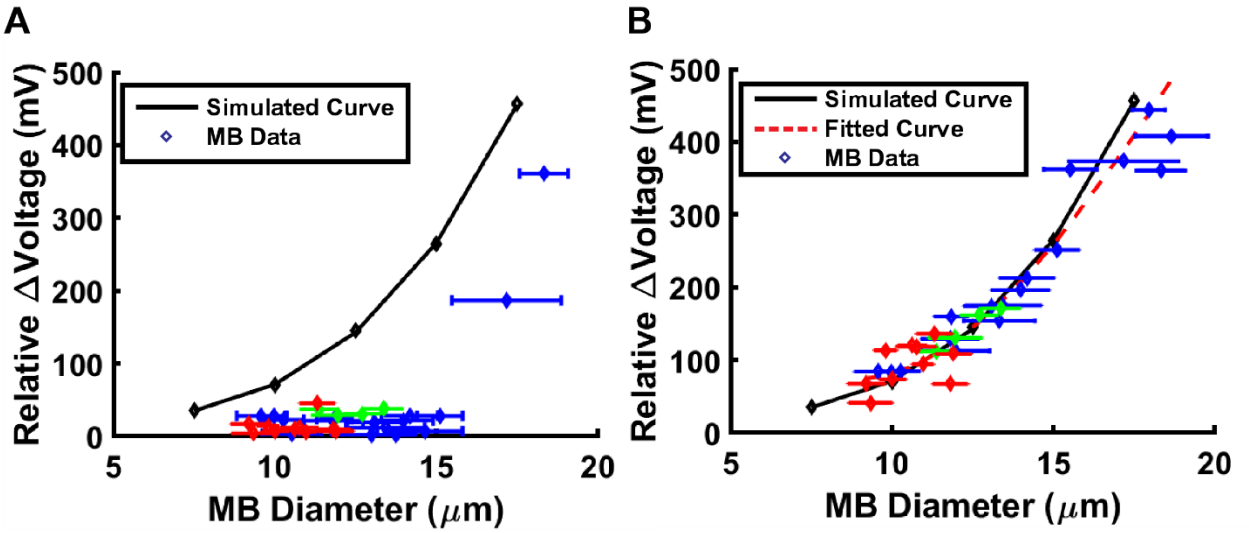

Figure 3.8 Plot showing the correlation between the microbubble (MB) diameter and the magnitude of the impedance magnitude change. The points along the curve were obtained from PSpice circuit simulations for microbubbles of different diameters. The data points were obtained from acquisitions of electrical data varying microbubble production rates and diameters. Error bars are not shown for voltage because the variance in voltage is so small that the error bars do not appear conspicuously in the figure. (A) Raw data. (B) Corrected data.

3.3.5 Estimation of microbubble diameter

After validating the compensation strategy introduced in Equations 2.4 and 2.5 and establishing a correction factor that scales with production rate, microbubbles were fabricated at different diameters and production rates and electrical and optical data were simultaneously acquired. Figure 3.9 illustrates electrically determined microbubble diameter versus optically determined microbubble diameter. The electrically observed diameters were corrected using the electrically determined microbubble production rate as an input to the compensation method, as described in 3.3.4. The figure illustrates that microbubbles of similar diameters and different productions rates still result in electrically determined diameters of an equivalent size, which was not achieved prior to the regression-based calibration operation, and demonstrates the agreement between the optical and electrical methods of measurement. A tight grouping along the diagonal line y = x denotes

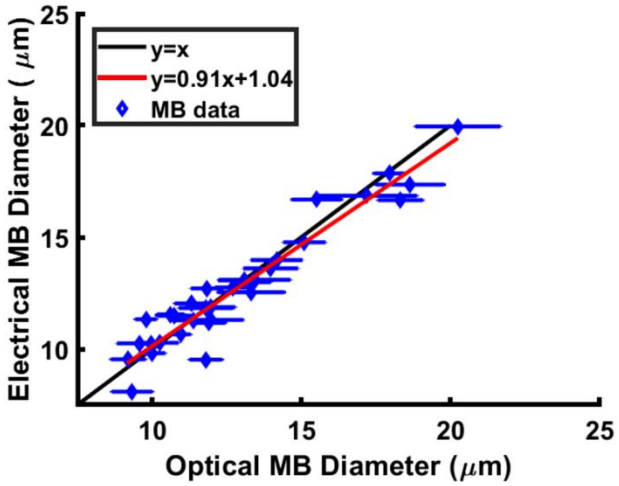

Figure 3.9 Comparison of methods to determine microbubble (MB) diameter. Optically determined microbubble diameter spans the x axis and electrically determined microbubble diameter the y axis. The black line is y=x and data points on that line demonstrates excellent agreement.

excellent agreement, R^2 = 0.91, between the two methods of microbubble detection. A coefficient of determination, R^2 = 0.93, follows the line y = 0.91x + 1.04. A plot of the residual values comparing optically determined diameter to the electrically determined diameter is reported in Figure 3.10.

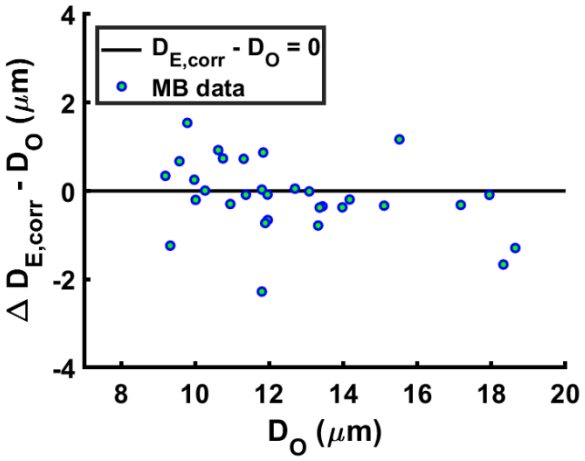

Figure 3.10 Residuals of the diameter are plotted.

3.4 Discussion

3.4.1 Device Performance

The results of this study demonstrate a μCPC integrated within the expanding nozzle of an FFMD capable of counting microbubbles up to 3.25 x 10^5 MB s^{-1} at sizes down to approximately 8 μm in diameter; parameters that meet, or exceed, projected needs relevant to our application. Measured noise indicates that the μCPC is capable of sensing microbubbles as small as 2.5 μm in diameter; however, only microbubbles of ≥ 8 μm were investigated in this study. To our knowledge, this is the first demonstration of sequential production and characterization of microbubbles by a μCPC integrated within the expanding nozzle of a flow focusing device at high throughput (> 1 x 10^4 MB s^{-1}). This strategy achieves a non-optical method of characterization that is low cost and portable for the analysis of benchtop FFMD microbubble production. The method has the potential to benefit *in vivo* research of FFMDs previously limited due to the constraints of high-speed optical microscopy. A primary example where this technology can be deployed is as a quality control system on a catheter tip measuring microbubbles administered for therapeutic benefit in various blood clot dissolution settings.[91] Further, this strategy extends to research involving the administration of liquid micro-droplets or other more exotic particles produced using an FFMD in which a material phase contrast in impedance magnitude is present. Ultimately, this strategy may prove clinically useful for sonothrombolysis in a blood clot dissolution setting. It achieves a quality control and safety assurance solution necessary for real-time control and verification of generated material as it is administered to patients.

This novel μCPC design benefits from unique features of FFMD-produced microbubbles. Foremost, when producing microbubbles at a high production rate, the electrical signals within the detection region from individual microbubbles superimpose to produce a combined signal that resembles that of a larger microbubble. However, as demonstrated by the analysis, individual microbubble signals were decoded from a signal featuring multiple microbubbles simultaneously within the detection region by detecting the relative, not absolute, change in signal. This compensation strategy is enabled by the high degree of similarity between sequentially produced monodisperse microbubbles within FFMDs. Under controlled conditions, the gas pinch-off mechanism at the nozzle results in the continuous generation of substantially equivalent microbubbles separated by equal distances. The data (Figure 3.8B) support results from Bernabini *et al.*, who reported a cubic polynomial change in the impedance magnitude with respect to particles of different radii.[80] The finding is expected as the volume of a sphere is governed by the third power of the radius. Conversely, conventional μCPC analysis of heterogeneous particles requires significant dilution of the particle-containing phase to prevent the occurrence of two or more multiply-sized particles simultaneously within the detection region. Thus, as a result of needing to dilute the particle-containing solution, high throughputs ($> 1 \times 10^4$ particles s^{-1}) are seldom achieved.

3.4.2 Limitations

Coplanar electrodes offer a simplified fabrication process relative to top-and-bottom electrodes and are commonly used for the fabrication of μCPCs. While coplanar electrode devices have been predominant in the literature, they suffer from decreased sensitivity due to a necessarily larger detection region than the top-and-bottom electrode configuration.[58]

Additionally, non-uniform current in the detection region causes an impedance magnitude modulation dependent on the height of the particle in channel. Spencer *et al*. recently demonstrated a post-processing algorithm to correct for height dependence using coplanar electrodes.[84]

At higher production rates, multiple microbubbles enter the detection region simultaneously and consequently decrease the relative amplitude modulation by interfering with each microbubble's measurement. However, this may be addressed by using a compensation strategy that corrects for the production rate or, conversely, the centre-to-centre distance between successively produced microbubbles. A complementary component to further enhance agreement in detection methods would include compiling a library of data on the device including liquid flow rates and gas pressures to produce microbubbles of certain diameters and production rates. Wang *et al*. constructed a library of microbubble production parameters using a FFMD that preceded this device.[102] Liquid phase flow rates and gas pressures were varied to encompass the various sizes and production rates that were achieved using the FFMD. Using the library of data similarly, with a given liquid phase flow rate, gas pressure, and production rate (electrically detected), a microbubble size could then be extracted. The study investigated various production regimes, including doublet and triplet production of microbubbles that yielded polydisperse populations.[102] The study presented here is constrained to monodisperse microbubbles produced sequentially. Since the proposed method cannot directly determine the presence of doublet or triplet formation, it is necessary to ensure that the operating parameters are outside of those consistent with the potential for doublet and triplet formation. In practice, this condition is easily met.

3.5 Conclusions

A benchtop FFMD with an integrated µCPC was fabricated and demonstrated *in situ* production and characterization of microbubbles; however, we envision broad utilization for characterization of liquid micro-droplets as well. The µCPC detected microbubbles using coplanar electrodes that were electrically excited with an AC signal. The passage of microbubbles within the detection region and confined by the electrodes created a modulation in the impedance magnitude between the two electrodes that was measurable. A calibration method was established that accounted for the interference resulting from the presence of multiple microbubbles in the detection region simultaneously. Experimental detection of microbubble populations of different sizes (8 – 20 µm diameter) and production rates (< 3.25×10^5 MB s^{-1}) were achieved and compared to simulated data and optical detection techniques. Results demonstrate excellent agreement ($R^2 = 0.91$) between electrical and optical detection. In conclusion, the system counts and measures the diameter of microbubbles at production rates as high as 3.25×10^5 MB s^{-1} and diameters between 8 and 20 µm.

Chapter 4. Conclusions and Future Directions

4.1 Conclusions

In this thesis, a benchtop FFMD with an integrated μCPC was fabricated and demonstrated *in situ* production and characterization of microbubbles. In chapter 2, simulations informed the design of the integrated electrode detection region and established the theoretical performance of the device and, in chapter 3, were validated by experimental data. Single microbubble simulations established the maximum impedance magnitude modulation within the detection region for microbubbles of diameters from 7.5 to 17.5 μm. Multi-microbubble simulations established the anticipated impedance magnitude modulation for microbubbles of a given diameter at variable production rates and established a relationship that was used to relate the optically determined centre-to-centre distance between successively produced microbubbles to a correction factor. Further, a calibration method was established that accounted for the interference resulting from the presence of multiple microbubbles in the detection region simultaneously. Experimental detection of microbubble populations of different sizes (8 – 20 μm diameter) and production rates ($< 3.25 \times 10^5$ MB s^{-1}) were achieved and validated against simulated data and optical detection techniques. Results demonstrate excellent agreement ($R^2 = 0.91$) between electrical and optical detection. In conclusion, the system counts and measures the diameter of microbubbles at production rates ($< 3.25 \times 10^5$ MB s^{-1}) and diameters (8 – 20 μm) that meet, or exceed, projected needs relevant to our application.

4.2 Future Directions

The work described in this thesis provided a proof of concept for the development of an *in situ* electrical detection system that functioned as a quality control mechanism in a benchtop FFMD-μCPC. There are two directions in which this project can advance. First, miniaturizing the device such that the electrical detection region can be incorporated into a catheter FFMD-μCPC with vascular compatible dimensions. Second, developing a control system for automatic initialization and real-time monitoring of operation will permit the use of FFMD-μCPCs in new investigative settings, such as *in situ* intravascular deployment, in the context of sonothrombolysis.

Peer Reviewed Journal Articles, Conference Abstracts and Presentations

Peer-reviewed and published articles:

1. AJ Dixon, **JMR Rickel**, B Shin, AL Klibanov, JA Hossack, "Acceleration of thrombolysis by ultrasound-stimulation of microbubbles produced by a microfluidic catheter." *Ann Biomed Eng*, 2018, **46**, 222-232.

2. **JMR Rickel**, AJ Dixon, AL Klibanov, JA Hossack. "A flow focusing microfluidic device with an integrated micro coulter particle counter for sequential production and characterization of size tunable microbubbles". *Lab Chip*, 2018, **18**, 2653 – 2664.

3. AJ Dixon, J Li, **JMR Rickel**, AL Klibanov, Z Zuo, JA Hossack, "Efficiency of sonothrombolysis using microbubbles produced by a catheter-based microfluidic device in a rat model of ischemic stroke". *Ann Biomed Eng.* 2019, https://doi.org/10.1007/s10439-019-02209-0

Conference Abstracts and Presentations

1. AJ Dixon, B Shin, V Meka, JP Kilroy, **JMR Rickel**, AL Klibanov, JA Hossack, "Large diameter microbubbles produced by a catheter-based microfluidic device for sonothrombolysis applications." IEEE International Ultrasonics Symposium, Oral by AJ Dixon, Taipei, Taiwan, 2015.

2. AJ Dixon, J Li, **JMR Rickel**, B Shin, Z Zuo, JA Hossack, "Sonothrombolysis efficacy of microbubbles produced by a microfluidic device in a rat ischemic stroke model." IEEE International Ultrasonics Symposium, Oral by AJ Dixon, Tours, France, 2016.

3. **JMR Rickel**, AJ Dixon, AL Klibanov, JA Hossack. "A flow focusing microfluidic device with an integrated micro coulter particle counter for sequential production and characterization of size tunable microbubbles." IEEE International Ultrasonics Symposium, Oral by JMR Rickel, Washington, DC, 2017.

4. Y Xie, AJ Dixon, **JMR Rickel**, JA Hossack, "Real time control of microbubble diameter from a flow focusing microfluidic device." IEEE International Ultrasonics Syposium, Oral by Y Xie, Glasgow, Scotland, 2019.

References

1. Ferrara, K., Pollard, R. & Borden, M. Ultrasound Microbubble Contrast Agents: Fundamentals and Application to Gene and Drug Delivery. *Annual Review of Biomedical Engineering* **9**, 415–447 (2007).

2. Klibanov, A. L. Microbubble Contrast Agents: Targeted Ultrasound Imaging and Ultrasound-Assisted Drug-Delivery Applications. *Investigative Radiology* **41**, 354–362 (2006).

3. Kotopoulis, S., Dimcevski, G., Helge Gilja, O., Hoem, D. & Postema, M. Treatment of human pancreatic cancer using combined ultrasound, microbubbles, and gemcitabine: A clinical case study: Clinical sonoporation setup for human pancreatic cancer. *Medical Physics* **40**, 072902 (2013).

4. Abou-Elkacem, L., Bachawal, S. V. & Willmann, J. K. Ultrasound molecular imaging: Moving toward clinical translation. *European Journal of Radiology* **84**, 1685–1693 (2015).

5. Burns, P. N., Wilson, S. R. & Simpson, D. H. Pulse inversion imaging of liver blood flow: improved method for characterizing focal masses with microbubble contrast. *Investigative Radiology* **35**, 58-71 (2000).

6. Chapman, C. S. & Lazenby, J. C. Ultrasound imaging system employing phase inversion subtraction to enhance the image. US5632277 A (1997).

7. Eckersley, R. J., Chin, C. T. & Burns, P. N. Optimising phase and amplitude modulation schemes for imaging microbubble contrast agents at low acoustic power. *Ultrasound in Medicine & Biology* **31**, 213–219 (2005).

8. Dhanaliwala, A. H., Dixon, A. J., Lin, D., Chen, J. L., Kibanov, A. L. & Hossack, J. A. In vivo imaging of microfluidic-produced microbubbles. *Biomedical Microdevices* **17**, (2015).

9. Borrelli, M. J. *et al*. Influences of Microbubble Diameter and Ultrasonic Parameters on In Vitro Sonothrombolysis Efficacy. *Journal of Vascular and Interventional Radiology* **23**, 1677-1684 (2012).

10. Leighton, T. G. *The Acoustic Bubble*. (Elsevier, 1994).

11. Brennen, C. E. *Cavitation and Bubble Dynamics*. (Oxford University Press, 1995).

12. Choi, J. J. Feshitan, J. A., Baseri, B., Wang, S., Tung, Y.-S. & Borden, M. A. Microbubble-Size Dependence of Focused Ultrasound-Induced Blood-Brain Barrier Opening in Mice In Vivo. *IEEE Transactions on Biomedical Engineering* **57**, 145–154 (2010).

13. Hölscher, T. *et al*. In vitro Sonothrombolysis with Duplex Ultrasound: First Results Using a Simplified Model. *Cerebrovascular Diseases* **28**, 365–370 (2009).

14. Hitchcock, K. E. *et al*. Ultrasound-Enhanced rt-PA Thrombolysis in an ex vivo Porcine Carotid Artery Model. *Ultrasound in Medicine & Biology* **37**, 1240–1251 (2011).

15. Porter, T. R., LeVeen, R. F., Fox, R., Kricsfeld, A. & Xie, F. Thrombolytic enhancement with perfluorocarbonexposed sonicated dextrose albumin microbubbles. *American Heart Journal* **132**, 964–968 (1996).

16. Weiss, H. L. *et al*. Mechanical clot damage from cavitation during sonothrombolysis. *The Journal of the Acoustical Society of America* **133**, 3159–3175 (2013).

17. Chuang, Y.-H., Cheng, P.-W. & Li, P.-C. Combining radiation force with cavitation for enhanced sonothrombolysis. *IEEE Transactions on Ultrasonics, Ferroelectrics, and Frequency Control* **60**, 97–104 (2013).

18. Shaw, G. J., Meunier, J. M., Huang, S.-L., Lindsell, C. J., McPherson, D. D. & Holland, C. K. Ultrasound-enhanced thrombolysis with tPA-loaded echogenic liposomes. *Thrombosis Research* **124**, 306–310 (2009).

19. Smith, D. A. B. *et al*. Ultrasound-Triggered Release of Recombinant Tissue-Type Plasminogen Activator from Echogenic Liposomes. *Ultrasound in Medicine & Biology* **36**, 145–157 (2010).

20. Petit, B. *et al.* In Vitro Sonothrombolysis of Human Blood Clots with BR38 Microbubbles. *Ultrasound in Medicine & Biology* **38**, 1222–1233 (2012).

21. Brown, A. T., Flores, R., Hamilton, E., Roberson, P. K., Borrelli, M. J. & Culp, W. C. Microbubbles Improve Sonothrombolysis In Vitro and Decrease Hemorrhage In Vivo in a Rabbit Stroke Model: *Investigative Radiology* **46**, 202–207 (2011).

22. Ferrara, K. W. Driving delivery vehicles with ultrasound. *Advanced Drug Delivery Reviews* **60**, 1097–1102 (2008).

23. Unnikrishnan, S. & Klibanov, A. L. Microbubbles as Ultrasound Contrast Agents for Molecular Imaging: Preparation and Application. *American Journal of Roentgenology* **199**, 292–299 (2012).

24. Hettiarachchi, K., Talu, E., Longo, M. L., Dayton, P. A. & Lee, A. P. On-chip generation of microbubbles as a practical technology for manufacturing contrast agents for ultrasonic imaging. *Lab on a Chip* **7**, 463 (2007).

25. Castro-Hernández, E., van Hoeve, W., Lohse, D. & Gordillo, J. M. Microbubble generation in a co-flow device operated in a new regime. *Lab on a Chip* **11**, 2023 (2011).

26. Garstecki, P., Gitlin, I., DiLuzio, W., Whitesides, G. M., Kumacheva, E. & Stone H. A. Formation Formation of monodisperse bubbles in a microfluidic flow-focusing device. *Applied Physics Letters* **85**, 2649 (2004).

27. Talu, E., Hettiarachchi, K., Powell, R. L., Lee, A.P., Dayton, P. A. & Longo, M. L. Maintaining Monodispersity in a Microbubble Population Formed by Flow-Focusing. *Langmuir* **24**, 1745–1749 (2008).

28. Garstecki, P., Fuerstman, M. J., Stone, H. A. & Whitesides, G. M. Formation of droplets and bubbles in a microfluidic T-junction-scaling and mechanism of break-up. *Lab on a Chip* **6**, 437–446 (2006).

29. Kaya, M., Feingold, S., Hettiarachchi, K., Lee, A. P. & Dayton, P. A. Acoustic responses of monodisperse lipid encapsulated microbubble contrast agents produced by flow focusing. *Bubble Science, Engineering & Technology* **2**, 33–40 (2010).

30. Chen, J. L., Dhanaliwala, A. H., Dixon, A. J., Klibanov, A. L. & Hossack, J. A. Synthesis and Characterization of Transiently Stable Albumin-Coated Microbubbles via a Flow-Focusing Microfluidic Device. *Ultrasound in Medicine & Biology* **40**, 400–409 (2014).

31. Dixon, A. J., Dhanaliwala, A. H., Chen, J. L. & Hossack, J. A. Enhanced Intracellular Delivery of a Model Drug Using Microbubbles Produced by a Microfluidic Device. *Ultrasound in Medicine & Biology* **39**, 1267–1276 (2013).

32. Dhanaliwala, A. H., Chen, J. L., Wang, S. & Hossack, J. A. Liquid flooded flow-focusing microfluidic device for in situ generation of monodisperse microbubbles. *Microfluidics and Nanofluidics* **14**, 457–467 (2012).

33. Chen, J. L., Dhanaliwala, A. H., Shiying Wang & Hossack, J. A. Parallel output, liquid flooded flow-focusing microfluidic device for generating monodisperse microbubbles within a catheter. *IEEE International Ultrasonics Symposium Proceedings*, 160–163 (2011).

34. Alexandrov, A. V. *et al.* Ultrasound-Enhanced Systemic Thrombolysis for Acute Ischemic Stroke. *New England Journal of Medicine* **351**, 2170–2178 (2004).

35. Molina, C. A. *et al.* Microbubble Administration Accelerates Clot Lysis During Continuous 2-MHz Ultrasound Monitoring in Stroke Patients Treated With Intravenous Tissue Plasminogen Activator. *Stroke* **37**, 425–429 (2006).

36. Alexandrov, A. V. *et al.* A Pilot Randomized Clinical Safety Study of Sonothrombolysis Augmentation With Ultrasound-Activated Perflutren-Lipid Microspheres for Acute Ischemic Stroke. *Stroke* **39**, 1464–1469 (2008).

37. Chen, X., Leeman, J. E., Wang, J., Pacella, J. J. & Villanueva, F. S. New Insights into Mechanisms of Sonothrombolysis Using Ultra-High-Speed Imaging. *Ultrasound in Medicine & Biology* **40**, 258–262 (2014).

38. Acconcia, C., Leung, B. Y. C., Hynynen, K. & Goertz, D. E. Interactions between ultrasound stimulated microbubbles and fibrin clots. *Applied Physics Letters* **103**, 053701 (2013).

39. Acconcia, C., Leung, B. Y. C., Manjunath, A. & Goertz, D. E. The Effect of Short Duration Ultrasound Pulses on the Interaction Between Individual Microbubbles and Fibrin Clots. *Ultrasound in Medicine & Biology* **41**, 2774-2782 (2015).

40. Acconcia, C., Leung, B. Y. C., Manjunath, A. & Goertz, D. E. Interactions between Individual Ultrasound-Stimulated Microbubbles and Fibrin Clots. *Ultrasound in Medicine & Biology* **40**, 2134–2150 (2014).

41. Saver, J. L. Improving reperfusion therapy for acute ischaemic stroke: Improving reperfusion therapy for acute stroke. *Journal of Thrombosis and Haemostasis* **9**, 333–343 (2011).

42. Tsivgoulis, G. *et al.* Safety and Efficacy of Ultrasound-Enhanced Thrombolysis: A Comprehensive Review and Meta-Analysis of Randomized and Nonrandomized Studies. *Stroke* **41**, 280–287 (2010).

43. Tsivgoulis, G. & Alexandrov, A. V. Ultrasound-enhanced thrombolysis in acute ischemic stroke: potential, failures, and safety. *Neurotherapeutics* **4**, 420–427 (2007).

44. Ribo, M., Molina, C. A., Alvarez, B., Rubiera, M., Alvarez-Sabin, J. & Matas, M. Intra-arterial Administration of Microbubbles and Continuous 2-MHz Ultrasound Insonation to Enhance Intra-arterial Thrombolysis. *Journal of Neuroimaging* **20**, 224–227 (2009).

45. Daffertshofer, M. *et al*. Transcranial Low-Frequency Ultrasound-Mediated Thrombolysis in Brain Ischemia: Increased Risk of Hemorrhage With Combined Ultrasound and Tissue Plasminogen Activator: Results of a Phase II Clinical Trial. *Stroke* **36**, 1441–1446 (2005).

46. Silverstein, M. D., Heit, J. A., Mohr, D. N., Petterson, T. M., O'Fallon, W. M. & Melton, L. J. Trends in the Incidence of Deep Vein Thrombosis and Pulmonary Embolism: A 25-Year Population-Based Study. *Archives of Internal Medicine* **158**, 585 (1998).

47. White, R. H. The Epidemiology of Venous Thromboembolism. *Circulation* **107**, 4I (2003).

48. Kearon, C. *et al*. Antithrombotic Therapy for VTE Disease. *Chest* **149**, 315–352 (2016).

49. Mannucci, P. M. & Poller, L. Venous thrombosis and anticoagulant therapy. *British Journal of Haematology* **114**, 258–270 (2001).

50. Baldwin, M. J., Moore, H. M., Rudarakanchana, N., Gohel, M. & Davies, A. H. Post-thrombotic syndrome: a clinical review. *Journal of Thrombosis and Haemostasis* **11**, 795–805 (2013).

51. Zhang, H., Chon, C. H., Pan, X. & Li, D. Methods for counting particles in microfluidic applications. *Microfluidics and Nanofluidics* **7**, 739–749 (2009).

52. Coulter, W. H. *US Patent* 2,656,508, 1953.

53. DeBlois, R. W. & Bean, C. P. Counting and Sizing of Submicron Particles by the Resistive Pulse Technique. *Review of Scientific Instruments* **41**, 909–916 (1970).

54. DeBlois, R. W. & Wesley, R. K. Sizes and concentrations of several type C oncornaviruses and bacteriophage T2 by the resistive-pulse technique. *J. Virol.* **23**, 227–233 (1977).

55. Koch, M., Evans, A. G. R. & Brunnschweiler, A. Design and fabrication of a micromachined Coulter counter. *Journal of Micromechanics and Microengineering* **9**, 159 (1999).

56. Anderson, J. R., Chiu, D. T., Wu, H., Schueller, O. J. & Whitesides, G. M. Fabrication of microfluidic systems in poly (dimethylsiloxane). *Electrophoresis* **21**, 27–40 (2000).

57. Sia, S. K. & Whitesides, G. M. Microfluidic devices fabricated in Poly(dimethylsiloxane) for biological studies. *ELECTROPHORESIS* **24**, 3563–3576 (2003).

58. Gawad, S., Schild, L. & Renaud, P. Micromachined impedance spectroscopy flow cytometer for cell analysis and particle sizing. *Lab on a Chip* **1**, 76 (2001).

59. Rodriguez-Trujillo, R., Mills, C. A., Samitier, J. & Gomila, G. Low cost micro-Coulter counter with hydrodynamic focusing. *Microfluidics and Nanofluidics* **3**, 171–176 (2006).

60. Jagtiani, A. V., Zhe, J., Hu, J. & Carletta, J. Detection and counting of micro-scale particles and pollen using a multi-aperture Coulter counter. *Measurement Science and Technology* **17**, 1706–1714 (2006).

61. Bayley, H. & Martin, C. R. Resistive-Pulse SensingFrom Microbes to Molecules. *Chemical Reviews* **100**, 2575–2594 (2000).

62. Kasianowicz, J. J., Brandin, E., Branton, D. & Deamer, D. W. Characterization of Individual Polynucleotide Molecules Using a Membrane Channel. *Proceedings of the National Academy of Sciences of the United States of America* **93**, 13770–13773 (1996).

63. Niu, X., Zhang, M., Peng, S., Wen, W. & Sheng, P. Real-time detection, control, and sorting of microfluidic droplets. *Biomicrofluidics* **1**, 044101 (2007).

64. Cheung, K. C., Di Berardino, M., Schade-Kampmann, G., Hebeisen. M., Pierzchalski, A. & Bocsi, J. Microfluidic impedance-based flow cytometry. *Cytometry Part A* **77A**, 648–666 (2010).

65. Kummrow, *et al.* Microfluidic structures for flow cytometric analysis of hydrodynamically focussed blood cells fabricated by ultraprecision micromachining. *Lab on a Chip* **9**, 972 (2009).

66. Simon, P., Frankowski, M., Bock, N. & Neukammer, J. Label-free whole blood cell differentiation based on multiple frequency AC impedance and light scattering analysis in a micro flow cytometer. *Lab on a Chip* **16**, 2326–2338 (2016).

67. Saleh, O. A. & Sohn, L. L. Quantitative sensing of nanoscale colloids using a microchip Coulter counter. *Review of Scientific Instruments* **72**, 4449–4451 (2001).

68. Lee, G.-B., Lin, C.-H. & Chang, G.-L. Micro flow cytometers with buried SU-8/SOG optical waveguides. *Sensors and Actuators A: Physical* **103**, 165–170 (2003).

69. Dong, T. & Barbosa, C. Capacitance Variation Induced by Microfluidic Two-Phase Flow across Insulated Interdigital Electrodes in Lab-On-Chip Devices. *Sensors* **15**, 2694–2708 (2015).

70. Yakdi, N. E., Huet, F. & Ngo, K. Detection and sizing of single droplets flowing in a lab-on-a-chip device by measuring impedance fluctuations. *Sensors and Actuators B: Chemical* **236**, 794–804 (2016).

71. Wei, K., Jayaweera, A. R., Firoozan, S., Linka, A., Skyba, D. M. & Kaul, S. Quantification of myocardial blood flow with ultrasound-induced destruction of microbubbles administered as a constant venous infusion. *Circulation* **97**, 473–483 (1998).

72. Errico, V., De Ninno, A., Bertani, F. R., Businaro, L., Bisegna P. & Caselli, F. Mitigating positional dependence in coplanar electrode Coulter-type microfluidic devices. *Sensors and Actuators B: Chemical* **247**, 580–586 (2017).

73. Pamme, N., Koyama, R. & Manz, A. Counting and sizing of particles and particle agglomerates in a microfluidic device using laser light scattering: application to a particle-enhanced immunoassay. *Lab on a Chip* **3**, 187 (2003).

74. Xiang, Q., Xuan, X., Xu, B. & Li, D. Multi-Functional Particle Detection with Embedded Optical Fibers in a Poly(dimethylsiloxane) Chip. *Instrumentation Science & Technology* **33**, 597–607 (2005).

75. Gawad, S., Cheung, K., Seger, U., Bertsch, A. & Renaud, P. Dielectric spectroscopy in a micromachined flow cytometer: theoretical and practical considerations. *Lab on a Chip* **4**, 241 (2004).

76. Cheung, K., Gawad, S. & Renaud, P. Impedance spectroscopy flow cytometry: On-chip label-free cell differentiation. *Cytometry Part A* **65A**, 124–132 (2005).

77. Sohn, L. L., Saleh, O. A., Facer, G. R., Beavis, A. J., Allan, R. S & Notterman, D. A. Capacitance cytometry: Measuring biological cells one by one. *Proceedings of the National Academy of Sciences* **97**, 10687–10690 (2000).

78. Murali, S., Xia, X., Jagtiani, A. V., Carletta, J. & Zhe, J. Capacitive Coulter counting: detection of metal wear particles in lubricant using a microfluidic device. *Smart Materials and Structures* **18**, 037001 (2009).

79. Carbonaro, A. & Sohn, L. L. A resistive-pulse sensor chip for multianalyte immunoassays. *Lab on a Chip* **5**, 1155 (2005).

80. Bernabini, C., Holmes, D. & Morgan, H. Micro-impedance cytometry for detection and analysis of micron-sized particles and bacteria. *Lab on a Chip* **11**, 407 (2011).

81. Lee, G.-B., Hung, C.-I., Ke, B.-J., Huang, G.-R., Hwei, B.-H. & Lai, H.-F. Hydrodynamic Focusing for a Micromachined Flow Cytometer. *Journal of Fluids Engineering* **123**, 672 (2001).

82. Nieuwenhuis, J. H., Kohl, F., Bastemeijer, J., Sarro, P. M. & Vellekoop, M. J. Integrated Coulter counter based on 2-dimensional liquid aperture control. *Sensors and Actuators B: Chemical* **102**, 44–50 (2004).

83. Wu, X., Kang, Y., Wang, Y.-N., Xu, D., Li, D, & Li, D. Microfluidic differential resistive pulse sensors. *ELECTROPHORESIS* **29**, 2754–2759 (2008).

84. Spencer, D., Caselli, F., Bisegna, P. & Morgan, H. High accuracy particle analysis using sheathless microfluidic impedance cytometry. *Lab on a Chip* **16**, 2467–2473 (2016).

85. Gawad, S., Sun, T., Green, N. G. & Morgan, H. Impedance spectroscopy using maximum length sequences: Application to single cell analysis. *Review of Scientific Instruments* **78**, 054301 (2007).

86. Sun, T., Berkel, C. van, Green, N. G. & Morgan, H. Digital signal processing methods for impedance microfluidic cytometry. *Microfluid Nanofluid* **6**, 179–187 (2009).

87. Xie, P., Cao, X., Lin, Z., Talukder, N., Emaminejad, S. & Javanmard, M. Processing gain and noise in multi-electrode impedance cytometers: Comprehensive electrical design methodology and characterization. *Sensors and Actuators B: Chemical* **241**, 672–680 (2017).

88. Song, Y., Yang, J., Pan, X. & Li, D. High-throughput and sensitive particle counting by a novel microfluidic differential resistive pulse sensor with multidetecting channels and a common reference channel: Microfluidics and Miniaturization. *ELECTROPHORESIS* **36**, 495–501 (2015).

89. Wood, D. K., Oh, S.-H., Lee, S.-H., Soh, H. T. & Cleland, A. N. High-bandwidth radio frequency Coulter counter. *Applied Physics Letters* **87**, 184106 (2005).

90. Fraikin, J.-L., Teesalu, T., McKenney, C. M., Ruoslahti, E. & Cleland, A. N. A high-throughput label-free nanoparticle analyser. *Nature Nanotechnology* **6**, 308–313 (2011).

91. Dixon, A. J., Rickel, J. M. R., Shin, B. D., Klibanov, A. L. & Hossack, J. A. In Vitro Sonothrombolysis Enhancement by Transiently Stable Microbubbles Produced by a Flow-Focusing Microfluidic Device. *Annals of Biomedical Engineering* **46**, 222–232 (2018).

92. Keller, M. W., Feinstein, S. B. & Watson, D. D. Successful left ventricular opacification following peripheral venous injection of sonicated contrast agent: an experimental evaluation. *American heart journal* **114**, 570–575 (1987).

93. Bardin, D., Martz, T. D., Sheeran, P. S., Shih, R., Dayton, P. A. & Lee, A. P. High-speed, clinical-scale microfluidic generation of stable phase-change droplets for gas embolotherapy. *Lab on a Chip* **11**, 3990 (2011).

94. Martz, T. D., Sheeran, P. S., Bardin, D., Lee, A. P. & Dayton, P. A. Precision Manufacture of Phase-Change Perfluorocarbon Droplets Using Microfluidics. *Ultrasound in Medicine & Biology* **37**, 1952–1957 (2011).

95. Prentice, P., Cuschieri, A., Dholakia, K., Prausnitz, M. & Campbell, P. Membrane disruption by optically controlled microbubble cavitation. *Nature Physics* **1**, 107–110 (2005).

96. van Wamel A., Kooiman, K., Harteveld., M., Emmer, M., ten Cate, F. J. & Versluis, M. Vibrating microbubbles poking individual cells: Drug transfer into cells via sonoporation. *Journal of Controlled Release* **112**, 149–155 (2006).

97. Dixon, A. J., Dhanaliwala, A. H., Chen, J. L. & Hossack, J. A. Enhanced Intracellular Delivery of a Model Drug Using Microbubbles Produced by a Microfluidic Device. *Ultrasound in Medicine & Biology* **39**, 1267–1276 (2013).

98. Berkhemer, O. A., et al. A Randomized Trial of Intraarterial Treatment for Acute Ischemic Stroke. *New England Journal of Medicine* **372**, 11–20 (2015).

99. Fritz, T. A., Unger, E. C., Sutherland, G. & Sahn, D. *Investigative Radiology **32***, 735-740 (1997).

100. Klibanov, A. L. Ultrasound Contrast Agents: Development of the Field and Current Status *Contrast Agents II*, 73-106 (2002).

101. Gañán-Calvo, A. M. & Gordillo, J. M. Perfectly Monodisperse Microbubbling by Capillary Flow Focusing. *Physical Review Letters* **87**, (2001).

102. Wang, S., Dhanaliwala, A. H., Chen, J. L. & Hossack, J. A. Production rate and diameter analysis of spherical monodisperse microbubbles from two-dimensional, expanding-nozzle flow-focusing microfluidic devices. *Biomicrofluidics* **7**, 014103 (2013).